JOURNAL OF GEOPHYSICAL RESEARCH, VOL. 102, NO. B8, PAGES 18,149–18,173, AUGUST 10, 1997

Devolatilization-generated fluid pressure and deformation-propagated fluid flow during prograde regional metamorphism

J. A. D. Connolly

Institute for Mineralogy and Petrography, Swiss Federal Institute of Technology, Zurich

Abstract. The obstruction to fluid flow formed by the rocks overlying a metamorphic devolatilization front causes the fluid pressure gradient in the reacting rocks to diverge from lithostatic. This drives deformation in tandem with the fluid pressure anomaly generated by the volume change of the reaction. Numerical simulations show that once the vertical extent of the reacted rocks is comparable to the compaction length, compaction processes caused by the difference between confining and fluid pressure gradients generate a positive fluid pressure anomaly (effective pressure < 0) above the reaction front, irrespective of the reaction volume change. Consequent dilational deformation propagates the anomaly upward, leading to underpressuring and densification at the reaction front and detachment of a wave of anomalous fluid pressure and porosity. Creep is a viable mechanism for such wave propagation for crustal viscosities $< 10^{15}$ MPa s. Continuous upward strengthening of the crust increases the wavelength and amplitude of the fluid pressure waves and thereby the likelihood of hydrofracture. Order of magnitude strength contrasts are adequate to arrest wave propagation, forming water sills that become increasingly stable in the absence of deviatoric stress. Although the fluid pressure gradient within a wave may be near hydrostatic, Rayleigh convection is unlikely. Thus, in the absence of lateral perturbations, fluid flow is upward and episodic, despite continuity of devolatilization. Porosity waves provide a mechanism for temporal focusing of metamorphic fluid fluxes with the potential to increase the efficacy of heat and mass transport.

Introduction

It is widely recognized that anomalous fluid pressure generated by metamorphic devolatilization reactions can have major consequences for rock strength, deformation style, and fluid flow patterns. Field evidence for lateral fluid flow [e.g., *Ferry,* 1987; *Skelton et al.,* 1995], crack-seal cycles [e.g., *Ramsay,* 1980], and fluid pressure oscillations [e.g., *Vrolijk,* 1987; *Fisher and Brantley,* 1992] all attest to the existence of anomalous fluid pressure in metamorphic environments. The difficulty of quantifying fluid pressure anomalies from field evidence provided the motivation for the study reported here in which the evolution of fluid pressure during midcrustal metamorphic devolatilization has been simulated with a numeric model.

Modeling devolatilization-generated fluid pressure is a problem that is inseparable from compaction and fluid flow. Much attention has been directed to modeling development of fluid overpressures relative to hydrostatic conditions [e.g., *Walder and Nur,* 1984; *Palciauskas and Domenico,* 1989; *Gavrilenko and Geugen,* 1993; *Hanson,* 1995]. Such studies typically account for the effects of dewatering reactions implicitly by incorporating a porosity production term in the governing equations used to describe fluid flow. These studies, in combination with those that have explicitly modeled reactions [e.g., *Bredehoft and Handshaw,* 1968; *Wong et al.,* 1997], have demonstrated that devolatilization is capable of generating substantial fluid overpressure and that compaction reduces crustal permeability and porosity rapidly relative to metamorphic timescales. This suggests, in accordance with conventional petrologic wisdom [e.g., *Fyfe et al.,* 1978], that at the onset of regional metamorphism, fluid pressure is either essentially equivalent to the confining pressure or that porosity is so low that negligible reaction progress is required to achieve lithostatic pressures. In contrast to the aforementioned studies, the purpose of the present study is to understand the evolution of a metamorphic system from such conditions.

Metamorphic reactions produce both fluid and a fraction of the porosity occupied by the fluid. In the limit that the fluid is not drained from the rock, that the ini-

Paper number 97JB00731.
0148-0227/97/97JB-00731$09.00

tial porosity is negligible, and that the rock matrix is rigid (i.e., isochoric), such reactions generate overpressures and hydrofracturing if the isobaric volume change for the reaction is positive [e.g., *Raleigh and Paterson,* 1965; *Yardley,* 1986]. Such a mechanism seems plausible provided the reaction occurs at conditions far from equilibrium so that pressure fluctuations do not alter the affinity for reaction [e.g., *Nishiyama,* 1989; *Yardley and Lloyd,* 1995], but during regional metamorphism, reactions are likely to occur at near equilibrium conditions. In this situation, fluid pressure may modulate reaction rates such that inelastic strain or fluid drainage hinders the development of any significant fluid pressure anomaly and consequent embrittlement. The nature of this modulation is evaluated here by considering the coupling of strain and reaction rates to fluid pressure.

In petrology, the assumption of lithostatic fluid pressure is often referred to as one of mechanical equilibrium, yet it is well known from fluid dynamics that the intermingling of two viscous fluids (e.g., a rock and its pore fluid) of differing density is inherently unstable in systems with hydraulic connectivity [e.g., *McKenzie,* 1984]. That metamorphic rocks have pore connectivity is demonstrated by lateral metamorphic fluid flow [e.g., *Ferry,* 1987; *Skelton et al.,* 1995] and evidence that rocks interact pervasively with externally derived fluids during metamorphism [e.g., *Valley and Graham,* 1991; *Chamberlain and Conrad,* 1991; *Young and Rumble,* 1993]. *Etheridge et al.* [1983] suggest that the lower crust consists of depth intervals where the fluid pressure gradient is hydrostatic, separated by impermeable barriers, a behavior similar to that observed in sedimentary basins [e.g., *Fyfe et al.,* 1978]. If there are domains of relatively high permeability within the crust, then the difference between the fluid and rock pressure gradients must lead to deformation, such that compaction and dilation occur at the bases and tops, respectively, of the domains; with the result that the domains must propagate upward [*Gold and Soter,* 1985]. For this reason, *Gold and Soter,* [1985] propose that fluid flow in the lower crust must be episodic in character, with fluid pressure oscillating about, or slightly below, the lithostat. From dimensional analysis, *Nur and Walder* [1992] argue that crustal dewatering occurs in hydraulic pulses of $10^3 - 10^5$ years duration. *Gold and Soter,* [1985] and *Nur and Walder* [1992] attribute a variety of seismic phenomena and ore-forming processes to episodic flow and review geologic evidence for this. The importance of episodic flow is widely appreciated with respect to melt segregation and transport, where analytic and numeric modeling has shown that pulsed flow through a deformable matrix can result from nonsteady state initial conditions [e.g., *Scott and Stevenson,* 1984; *Barcilon and Richter,* 1986; *Spiegelman,* 1993a].

The spatial and temporal scale of episodic flow is critically dependent on the rheology and permeability of the rock matrix [*McKenzie,* 1984] and on the magnitude of the perturbation to steady state flow conditions [e.g., *Spiegelman,* 1993b], i.e., in the context of the present problem the rate of fluid production. Accordingly, the first sections of this paper develop models for the conditions and rates of regional metamorphic devolatilization, the manner in which porosity dilates (or compacts) in response to the perturbation in fluid pressure caused by devolatilization, and the influence of this dilation on rock permeability. The interdependencies among these processes are then evaluated within the context of a numerical model.

Model Devolatilization Reactions

To obtain a general model for the devolatilization of the crust, phase relations were computed as a function of pressure and temperature for an average pelitic shale

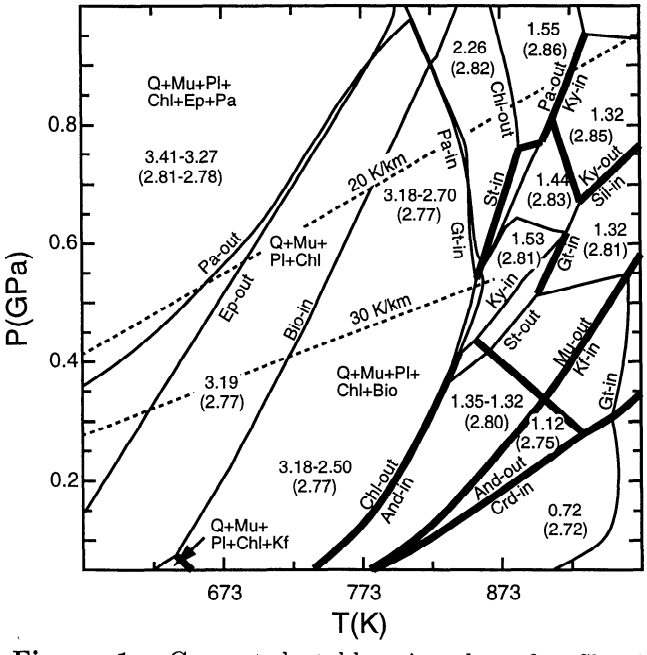

Figure 1. Computed stable mineralogy for *Shaw's* [1956] average metapelite composition (see Table 1 for computational and compositional details). Thin solid lines indicate conditions at which minerals appear or disappear, with increasing temperature, due to a continuous reaction. Heavy solid lines locate discontinuous reactions whereby one mineral is replaced by another. Representative water content (wt %), and density (g/cm^3) of the stable mineralogy are indicated in each region. Dashed curves locate geotherms for $\rho_r = 2.8\,\mathrm{g/cm^3}$. Phase notation and compositions considered are: And/Ky/Sill (andalusite/kyanite/sillimanite, Al_2SiO_5), Bio (biotite, $KMg_{(3-y)x}Fe_{(3-y)(1-x)}Al_{1+2y}Si_{3-y}O_{10}(OH)_2$), Chl (chlorite, $Mg_{(5-y)x}Fe_{(5-y)(1-x)}Al_{4+2y}Si_{3-y}O_{10}(OH)_8$), Crd (cordierite, $Mg_{2x}Fe_{2-2x}Al_4O_{10}$), Ep (epidote, $Ca_2Al_{3-x}Fe_xSi_3O_{12}(OH)$), Gt (garnet, $Fe_{3x}Ca_{3y}Mg_{3(1-x-y)}Al_2Si_3O_{12}$), Kf (K-feldspar, $K_xNa_{1-x}AlSi_3O_8$), Mu (muscovite, $K_xNa_{1-x}Mg_yFe_zAl_{3-2(y+z)}Si_{3+y+z}O_{10}(OH)_2$), Pa (paragonite, $Na_xK_{1-x}Al_3Si_3O_{10}(OH)_2$), Pl (plagioclase, $Na_xCa_{1-x}Al_{2-x}Si_{2+x}O_8$), Q (quartz, SiO_2), and St (staurolite, $Mg_{4x}Fe_{4-4x}Al_{18}Si_{7.5}O_{48}H_4$).

Table 1. Common Symbols and Characteristic Parameter Values

Symbol	Meaning	Units	Value
C_f	fluid heat capacity	$J\,kg^{-1}\,K^{-1}$	4×10^3
C_r	rock specific heat	$J\,m^{-3}\,K^{-1}$	2.5×10^6
k, k_0	permeability (equation (7)), initial value	m^2	$10^{-21} - 10^{-23}$
K	thermal conductivity	$W\,m^{-1}\,K^{-1}$	2.25
n_ϕ	porosity exponent (equation (7))	none	3
p_f, p_e	fluid pressure, effective pressure ($\rho_r gz - p_f$)	MPa	
q, q_0	fluid mass flux, initial (background) value	$kg\,m^{-2}\,s^{-1}$	$-1 \times (10^{-12} - 10^{-11})$
q_{ss}	steady state dehydration-generated fluid flux	$kg\,m^{-2}\,s^{-1}$	$-1 \times (10^{-9} - 10^{-8})^a$
$\dot{r}$	reaction fluid mass production rate (equation (2))	$kg\,H_2O\,m^{-3}\,s^{-1}$	
$\dot{r}_H$	reaction enthalpy production rate($\dot{r}\Delta H$)	$J\,m^{-3}\,s^{-1}$	
$\dot{r}_V$	reaction volume production rate ($\dot{r}\Delta V_s$)	s^{-1}	
R	gas constant		
R	fluid mixing ratio (equation (12))	none	
U	quantity characterizing wave propagation (equation (19))	none	
v_0	initial fluid velocity ($q_0/\phi_0/\rho_f$)	$m\,s^{-1}$	$-1 \times (10^{-12} - 10^{-10})$
v_{ss}	steady state (vertical) reaction front velocity	$m\,Myr^{-1}$	$-1 \times (10^2 - 10^3)$
w_{H_2O}	water released by dehydration	$kg\,H_2O\,m^{-3}$	36.1^a
β	fluid compressibility, $(1/\rho_f)(\partial\rho_f/\partial p)$	MPa^{-1}	0.7×10^{-3}
β_T	fluid expansivity, $(1/\rho_f)(\partial\rho_f/\partial T)$	K^{-1}	6.7×10^{-4}
z	depth coordinate	m	
δ	compaction length (equation (6)) $\sqrt{k(\zeta + 4/3\eta)/\mu}$	m	
ΔG	reaction Gibbs energy	$J/kg\,H_2O$	Table 3
ΔH	reaction enthalpy	$MJ/kg\,H_2O$	Table 3
ΔV	(isobaric) reaction volume change	$m^3/kg\,H_2O$	Table 3
ΔV_s	(isobaric) reaction solid volume change	$m^3/kg\,H_2O$	Table 3
$\Delta\phi$	porosity wave amplitude ($\phi_1 - \phi_0$)		
$\Delta\rho$	$\rho_r - \rho_f$	$kg\,m^{-3}$	2.015×10^3
η	rock shear viscosity	MPa s	$10^{13} - 10^{15}$
λ_p, λ_ϕ	p_f and ϕ anomaly wavelength (Table 5)		
κ	thermal diffusivity	$m^2\,s^{-1}$	1.1×10^{-6}
μ	fluid viscosity	MPa s	10^{-10}
ϕ, ϕ_0	porosity, initial (background) porosity		0.05-0.2
ϕ_1	maximum ϕ of a porosity wave		
$\phi*$	ϕ necessary to acommodate $q_{ss} + q_0$ by steady flow		
ρ_f	fluid density	$kg\,m^{-3}$	0.785×10^3
ρ_r	rock density	$kg\,m^{-3}$	2.8×10^3
ζ	rock bulk viscosity (equation (5))	MPa s	
ω	$k - \phi$ proportionality constant (equation (7))	m^2	10^{-13}

[a]Values for Chl ⇒ Ky dehydration, with thermally controlled steady state rates.

composition. The resulting petrogenetic grid (Figure 1, see Table 1 for parameter notation and Table 2 for phase notation and mineral modes) is divided in two distinct regions by the chlorite dehydration equilibrium at ~773 K. Below 773 K, devolatilization is characterized by continuous reactions that release ~0.25 wt % fluid/100 K. At higher temperatures devolatilization occurs in pulses separated by intervals of relatively minor continuous devolatilization. The chlorite decomposition reaction corresponds to the largest of these pulses, releasing 1.1–1.3 wt % water, and has therefore been selected as the primary basis for subsequent modeling.

For geotherms >26 K/km, chlorite decomposition is univariant and forms either kyanite or andalusite by the reaction

$$\text{Chl} + \text{Mu} = \text{Bio} + \text{Q} + \text{And/Ky} + \text{H}_2\text{O}.$$

At higher pressures attained for geotherms < 24K/km, the reaction is not strictly univariant but occurs over such a narrow temperature interval that it is well approximated as

$$\text{Chl} + \text{Pl} + \text{Mu} = \text{Bio} + \text{Q} + \text{Gt} + \text{H}_2\text{O}$$

where garnet appears at the expense of chlorite. For brevity these reactions are referred to the Chl ⇒ Ky and Chl ⇒ Gt reactions. There is a narrow pressure interval between the Chl ⇒ Ky and Chl ⇒ Gt fields, where staurolite forms from chlorite (Chl ⇒ St).

The metapelite mineralogies, water contents, and densities of Figure 1 agree with petrographic observations [e.g., *Schmid*, 1979]. This phase diagram section thus represents a useful schematic of pelite devolatilization, but its significance should not be overestimated.

Table 2. Computed Mineral Modes and Compositions, Density (at Zero Porosity), and Water Content for *Shaw's* [1956] Average "High-Grade" Metapelite at 300 and 700 MPa

	T K					
	673	773	823	873	878	893
			P = 300 MPa			
And			5.56			7.03
Bio		8.81 $Bio_{40,40}$	25.91 $Bio_{39,44}$			26.13 $Bio_{38,44}$
Chl	15.51 $Chl_{39,18}$	11.45 $Chl_{40,40}$				
Mu	28.06 $Mu_{70,10,20}$	19.93 $Mu_{90,0,10}$	4.59 $Mu_{90,0,10}$			
Q	32.53	35.78	39.33			38.80
Pl	23.8 Pl_{73}	24.03 Pl_{73}	24.62 Pl_{73}			23.99 Pl_{73}
Kf						4.05 Kf_{82}
ρ_r	2.77×10^3	2.77×10^3	2.80×10^3			2.80×10^3
H_2O	3.19	2.70	1.32			1.12
			P = 700 MPa			
Bio			0.30 $Bio_{31,25}$	13.59 $Bio_{49,40}$	17.83 $Bio_{49,40}$	
Chl	15.14 $Chl_{40,11}$	15.51 $Chl_{40,17}$	15.37 $Chl_{40,20}$	3.10 $Chl_{50,40}$		
Ep	3.23 Ep_{25}					
Gt				4.63 $Gt_{5,13,82}$	3.85 $Gt_{5,13,82}$	
Mu	28.10 $Mu_{70,10,20}$	28.06 $Mu_{90,0,10}$	27.79 $Mu_{70,10,20}$	15.32 $Mu_{90,0,10}$	11.63 $Mu_{90,0,10}$	
Q	33.33	32.53	32.64	37.17	38.22	
Pa	3.16 Pa_{95}			5.99 Pa_{86}	5.57 Pa_{86}	
Pl	17.04 Pl_{91}	23.90 Pl_{73}	23.90 Pl_{73}	20.19 Pl_{71}	20.75 Pl_{71}	
St					2.16 St_{10}	
ρ_r	2.80×10^3	2.77×10^3	2.77×10^3	2.83×10^3	2.84×10^3	
H_2O	3.35	3.19	3.18	1.93	1.60	

Mineral modes are in volume percent. Molar (nonvolatile) chemical composition is 3.16 Na_2O, 5.73 MgO, 17.0 Al_2O_3, 105.7 SiO_2, 3.56 K_2O, 2.21 CaO, 9.05 FeO. Redox state and volatile composition of the rock are determined by imposing the constraint that the rock is equilibrated with water and graphite [*Connolly and Cesare,* 1993]. Stable phase assemblages were computed as a function of pressure and temperature using the PERPLEX program [*Connolly,* 1990], thermodynamic data [*Holland and Powell,* 1990], and solution models used by *Connolly et al.* [1994]. Mineral compositions indicated by the subscripts on mineral names; these correspond to the x, y, and z coefficients (in percent) of the formulas listed in the Figure 1 caption.

Low-grade metapelites commonly contain ~2 wt % CO_2 [*Shaw,* 1956]. Decarbonation raises fluid production rates over those estimated here and may increase the variance of devolatilization, lessening the importance of discontinuous reactions. These effects are maximized at low temperature. Conditions for low-temperature continuous reactions are also sensitive to bulk composition. In contrast, the high-temperature discontinuous reactions of Figure 1 are relevant for a wider range of pelitic compositions, although the amount of water and porosity generated by the reactions varies with bulk composition.

Although there is invariably a reduction in solid volume (ΔV_s) associated with devolatilization, the total volume change (ΔV) varies from positive to negative with increasing pressure. This effect has been ascribed

Table 3. Discontinuous Reaction Properties

Reaction	ν_{RLM}	a, J/mol	b, J/mol/K	c, J/MPa/mol	ΔH, MJ/kg H_2O	ΔV_s, m^3/kg H_2O	ΔV, m^3/kg H_2O	V_{RLM}, %
Chl⇒And/Ky	0.613	79788	-152.09	-0.113	2.9	-5.9×10^{-4}	7.5×10^{-4}	6.16
Chl⇒Gt	0.552	75445	-139.92	-0.238	2.5	-1.3×10^{-3}	-1.6×10^{-5}	5.17

A mole of reaction is defined as the quantity necessary to liberate one mole of H_2O. ΔG is computed as $\Delta G = a + bT + cp_f + RT \ln f^*_{H_2O}$, where $f^*_{H_2O}$ is the water fugacity of water equilibrated with graphite [*Connolly and Cesare,* 1993]. ΔV_s is the solid volume change. ΔV is the (fluid+rock) isobaric volume change. For the discontinuous dehydration models dehydration releases 36.4 kg H_2O/m^3 rock (1.3 wt %H_2O). V_{RLM} is the final mode of the rate limiting mineral produced by the dehydration. The porosity that must be generated for the dehydration to occur isobarically is $w_{H_2O}(\Delta V_{tot} - \Delta V_s)$, ~4%.

considerable mechanical importance [e.g., *Nishiyama,* 1989]. Positive ΔV reactions are thought to cause fluid overpressuring and hydrofracture, whereas reactions with negative ΔV are thought to cause underpressuring and therefore to be incapable of inducing embrittlement. The sign of ΔV for an equilibrium is manifest by the sign in the Clapeyron slope of the corresponding phase field; thus the Chl $\Rightarrow$ Ky and Chl $\Rightarrow$ Gt reactions represent these two scenarios. The Chl $\Rightarrow$ St reaction has an intermediate, near-zero, isobaric volume change; this reaction is not considered further because its behavior is between the extremes represented by the Chl $\Rightarrow$ Ky and Chl $\Rightarrow$ Gt reactions.

The stoichiometries of the Chl $\Rightarrow$ Ky and Chl $\Rightarrow$ Gt reactions vary as a function of pressure, but the changes in solid volume, enthalpic requirements, and the amount of water released are not subject to important variations and are reasonably approximated by constants (Table 3).

Continuous Dehydration: Chl $\Rightarrow$ Bio

In some lithologies, fluid production is largely by continuous reactions. It can also be argued that the effect of crustal heterogeneity is to make the overall process of metamorphic devolatilization continuous. The continuous dehydration of chlorite to produce biotite (Figure 1) is used to simulate these situations. This reaction (Chl $\Rightarrow$ Bio) consumes 40 kJ/m^3 rock and liberates 0.5 wt % fluid uniformly over a 170 K interval commencing at $T = 623 + 0.1\,p_f$. To illustrate the behavior of a $\Delta V = 0$ reaction, ΔV for Chl $\Rightarrow$ Bio is taken to be zero (i.e., $\Delta V_s = 0.0178$ m^3/m^3 rock), although, in fact, there is a small positive ΔV for the reaction.

Devolatilization Kinetics

Reaction rates are fundamentally determined by chemical affinity, a measure of the displacement of the physicochemical conditions of a system from those of equilibrium. In a system where fluid pressure may vary independently of confining pressure, it is difficult to formulate a rigorous definition of chemical affinity. However, it has been argued that in nonhydrostatic systems reaction occurs predominantly at mineral-fluid interfaces and that strain energy is negligible along these interfaces [*Ganguly,* 1977; *Bruton and Helgeson,* 1983; *Dahlen,* 1992]. In this case, the thermodynamic "pressure" is that of the fluid and the change in the Gibbs energy (ΔG) is the chemical affinity of the reaction, provided none of the chemical potentials of the system are subject to external control. Consequently, in an equilibrium system, the rate of reaction is determined by the rates at which heat and fluid flow affect ΔG through the relation

$$\Delta G = \Delta V \mathrm{d}p_f - \Delta S \mathrm{d}T \qquad (1)$$

where ΔS, the entropy change of the reaction, and ΔV are weak functions of fluid pressure and temperature. In the limit that a metamorphic reaction front is undrained and that rocks have finite strength, the perturbation to fluid pressure caused by the reaction will be opposite in sign to the volume change of the reaction. To maintain equilibrium, (1) requires a compensating temperature perturbation of $\delta T = (\Delta S/\Delta V)\delta p_f$. For nonequilibrium kinetics this implies that reaction-induced fluid pressure perturbations retard devolatilization. Likewise, from (1), drainage must accelerate $\Delta V > 0$ reactions, quench $\Delta V < 0$ reactions, and have no effect on the rate of isochoric reactions.

Models of prograde metamorphic reactions [e.g., *Lasaga,* 1986; *Ridley,* 1986] suggest that chemical kinetics are of minor importance for regional metamorphic timescales, but these models did not account for pressure effects. In the limit of equilibrium devolatilization in an isobaric system, a univariant reaction front has zero width, which implies that the strain rate induced by the volume change of the reaction must be infinite. For this reason at the outset of this study it was thought necessary to incorporate the nonequilibrium model for the Chl $\Rightarrow$ Ky and Chl $\Rightarrow$ Gt reactions described in Appendix A, based on *Lasaga and Rye* [1993]. In this model the devolatilization rate (kg H_2O/m^3 rock/s) is

$$\dot{r} = Mc|\Delta G|^{n_r} A_{RLM} \qquad (2)$$

where c is a temperature dependent rate constant, M is a reaction specific stoichiometric constant, n_r is an empirical constant, and A_{RLM} is the surface area of the rate limiting mineral (garnet or aluminosilicate). The parameterization of this model (Appendix A) determines the width of the incipient reaction front but has no influence on the subsequent fluid pressure evolution, during which reaction rates are essentially those of equilibrium. The relevance of the chemical kinetic model for the continuous Bio $\Rightarrow$ Chl reaction is questionable because of the absence of a refractory phase in the reaction. Thus Bio $\Rightarrow$ Chl reaction rates were estimated so as to maintain the temperature within an arbitrarily specified increment (0.01 K) of equilibrium.

Reaction-Generated Deformation

A metamorphic reaction acts as a chemical source of porosity, producing porosity by reducing the solid volume at a rate of $\dot{r}\Delta V_s$. At the same time, deformation may cause the pore structure of the rock to dilate or collapse due to a difference between pore and confining pressure. This deformation may be brittle, elastic, or inelastic. On the timescale of regional metamorphism, elastic compaction is likely to be negligible in comparison to that by plastic creep [e.g., *Palciauskas and Domenico,* 1989; *Hanson,* 1995] and is not considered further here. Microcracking is more problematic. *Gavrilenko and Geugen* [1993] argue that preexisting microcracks are closed and healed at depths > 15 km; thus the generation of new microcracks only occurs once

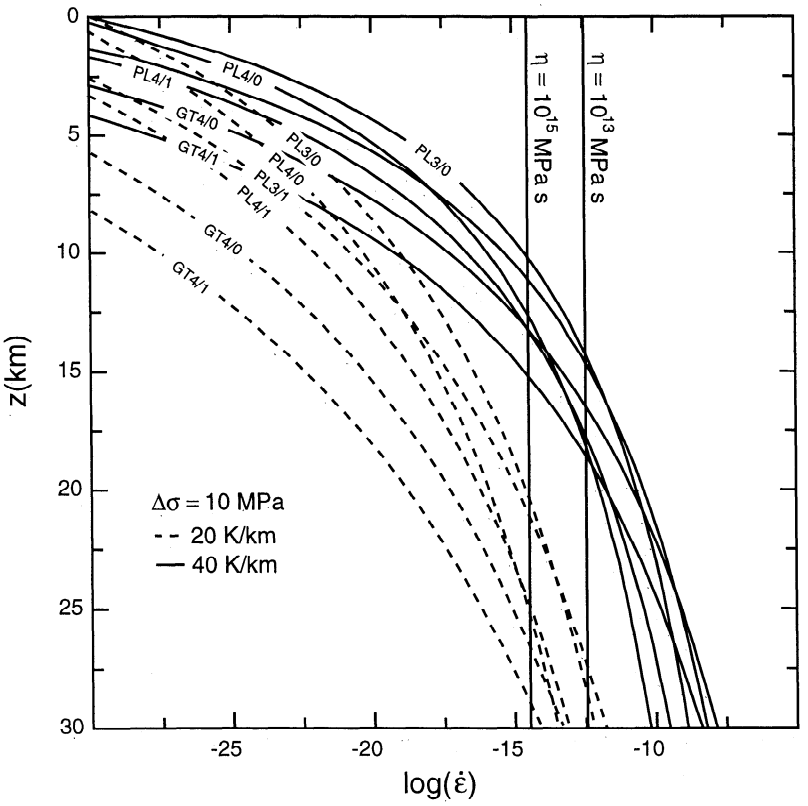

Figure 2. Strain rates for a flow stress of 10 MPa, parameters as given in Table 4 for power law creep rheologies. Dashed and solid curves are for geotherms of 20 and 40 K/km. Each curve is labeled by the corresponding model abbreviation and water fugacity exponent (m) given in Table 4. Vertical lines indicate strain rates for Newtonian rheologies of $\eta = 10^{13} - 10^{15}$ MPa s.

fluid pressure exceeds the confining pressure by some finite amount. The magnitude of this excess pressure may be $> 10^2 - 10^3$ MPa [*Raj and Ashby,* 1975; *Wanamaker et al.,* 1990], but a minimum value of 10–50 MPa is provided by measured rock strength in tension [*Geugen and Palciauskas,* 1994]. Intergrain and intragrain microcracking occurs with equal frequency in reaction-generated microcracking experiments, suggesting that grain boundaries have substantial strength [*Connolly et al.,* 1997]. Unless or until this strength is overcome, deformation is accomplished by creep and it is this stage of deformation that is investigated here.

Crustal Rheology

Two rheologic models are employed here for the crust: constant shear viscosity; and power law creep. While in detail the crust cannot be treated as a constant shear viscosity Newtonian fluid, tectonic behavior is broadly consistent with viscosities of $10^{13} - 10^{15}$ MPa s [e.g., *Ranalli,* 1986; *Hacker et al.,* 1992; *Kaufman and Royden,* 1994]. The utility of a constant shear viscosity model is both its simplicity and its avoidance of the uncertainty associated with extrapolation of experimental data to geologic conditions. Following *Brace and Kohlstedt* [1980], experimentally determined quartzite power law rheologies have been widely applied as an analog for crustal rheology. The axial strain rate of quartzite rheologies is adequately represented by the Dorn equation [*Paterson,* 1989]

$$\dot{\epsilon} = SDf_{H_2O}^m |\sigma|^n \exp\left(\frac{-Q}{RT}\right) \tag{3}$$

where D, n, m, and Q are empirical constants, f_{H_2O} is water fugacity and S is the sign of the flow stress σ. For a flow stress of 10 MPa (the magnitude of reaction-generated fluid pressure anomalies) and geothermal gradients characteristic of regional metamorphism (25–35 K/km), alternative experimental rheologies, and assumptions regarding their dependence on f_{H_2O}, cause 2–3 orders of magnitude variation in $\dot{\epsilon}$ at a depth of 20 km (Figure 2). This variation is minor in comparison to that due to a 10 K/km change in the geothermal gradient. Thus temperature is the dominant factor controlling rheologic response. Given that the Chl ⇒ Ky and Chl ⇒ Gt reactions occur at similar temperature, both take place in similar rheologic environments.

The rheological effect of water fugacity is most pronounced at shallow depths (Figure 2) where other deformation mechanisms are likely to operate [*Rutter,* 1976]. Although the difference between the activation energies determined by *Gleason and Tullis* [1995] and *Paterson and Luan* [1990] is significant, for the specific $p_f - T$

Table 4. Quartz Dislocation Creep Rheological Parameters ($m = 0$, Equation (3))

Rheology	Source	D, MPa^{n-m}	Q, kJ/mol	n
PL3	*Paterson and Luan* [1990]	$6.5 \times 10^{-8}(2.2 \times 10^{-10})$	135	3.1
PL4	*Paterson and Luan* [1990]	$4.0 \times 10^{-10}(1.4 \times 10^{-12})$	135	4
GT	*Gleason and Tullis* [1995]	$1.1 \times 10^{-4}(2.4 \times 10^{-8})$	223	4

From empirical analysis *Kohlstedt et al.* [1995] and *Gleason and Tullis* [1995] estimate $m = 1$ for equation (3), this is consistent mechanistic models ($1 \leq m \leq 2$)[*Paterson,* 1989]. D values for $m = 1$ are listed in parentheses (f_{H_2O} from *Haar et al.* [1984]).

conditions considered here, the PL4 and GT rheologies (Table 4) are virtually identical. Consequently GT is not considered further. The constant shear viscosity model is broadly consistent with the power law creep rheologies at crustal depths of ~20 km (Figure 2).

It is commonly accepted that pressure solution [*Rutter,* 1976] is the dominant creep mechanism at shallow levels in the crust [e.g., *Etheridge et al.,* 1983; *Gavrilenko and Geugen,* 1993]. However, high quartz-water dihedral angles [*Holness,* 1993] and low pore connectivity may inhibit this mechanism. Pressure solution creep is, in any case, poorly constrained by experimental data [*Gratz,* 1991], but it is Newtonian and often simulated by constant shear viscosity (e.g., *Birchwood and Turcotte* [1994] estimate a shear viscosity of 5×10^{14} MPa s for pressure solution controlled deformation in sedimentary basins). Given the small changes in mineral modes caused by the metapelite reactions (Figure 1 and Table 2), superplasticity [e.g., *Rutter and Brodie,* 1995] and grain size variations are unlikely to have significant rheologic consequences during metamorphism of pelitic rocks.

Compaction by Creep

The modeling of the collapse of underpressured porosity in an incompressible solid by creep is a subject that has been treated extensively in material science [e.g., *Ashby,* 1988]. This modeling relates the rate of porosity production to the isochoric axial strain rate of the solid. The resulting relationships depend on the geometry and amount of the porosity, the distribution of pore sizes, and the creep mechanism. In the specific case of power law creep the absolute pore size is unimportant and compaction tends to occur preferentially in bigger pores and should therefore lead to uniformity of pore sizes [*Ashby,* 1988]. In texturally equilibrated rocks, experimental studies of fluid-mineral dihedral angles indicate that when hydraulic connectivity exists, the hydraulic bonds are most likely to be grain-edge channels [e.g., *Holness,* 1993]. For the approximation that these channels are represented as cylindrical tubes, *Wilkinson and Ashby* [1975] give the porosity (ϕ) production rate by power law creep as

$$(1-\phi)\frac{d\phi}{dt} = -SA\,2^{n+1}\frac{\phi(1-\phi)}{[1-\phi^{1/n}]^n}\left(\frac{|p_e|}{n}\right)^n \qquad (4)$$

where p_e is the effective pressure, and $A = Df_{H_2O}^m \exp(-Q/(RT))$, as in (3). In this paper the $1-\phi$ term on the left-hand side of (4) is neglected; this is an arithmetic simplification with minor physical effect because of the small porosities of interest.

A significant component of porosity may occur at quadruple grain junctions [e.g., *Beere,* 1975; *Waff and Faul,* 1992]. If this porosity were approximated as isolated spheres then the dilational strain rate would differ by a factor of only $(3/4)^{n+1}$ [*Wilkinson and Ashby,* 1975]. Equation (4) expresses porosity production in terms of $\dot{\epsilon}$, where the proportionality is a function of ϕ and n. For stress exponents characteristic of quartzites (3–4), and porosities of 0.001–0.1%, porosity production is an order of magnitude less than $\dot{\epsilon}/\phi$. Equation(4) is derived by assuming that grain shape does not change significantly during compaction; this assumption becomes questionable for $\phi > 10\%$, values unlikely to be realized in regional metamorphism. In the limit of a Newtonian dislocation creep rheology, (4) gives the bulk viscosity ζ as a function of the shear viscosity η

$$\zeta = \frac{3}{4}\frac{\eta}{\phi}. \qquad (5)$$

Equation (5) applies to diffusion creep at constant grain size, but for pressure solution a weaker dependence on porosity is obtained ($\zeta = 3\eta/(4\sqrt{\phi})$), [*Helle et al.,* 1985]. Porosity reduction by pressure solution in the Earth's crust occurs rapidly in comparison to metamorphic timescales. For example, for $\eta = 5 \times 10^{14}$ MPa s and an initial porosity of 10%, under drained conditions (i.e., a near hydrostatic fluid pressure gradient) the porosity would be reduced by 2 orders of magnitude within 5 km of the Earth's surface in <1 Myr. This timescale limits the duration of downward fluid flow within the Earth's crust because the existence of underpressured porosity is a necessary condition for downward fluid flow.

As postmetamorphic porosities and metamorphic porosities in the absence of reactions are <0.1% [e.g., *Norton and Knapp,* 1977; *Bickle and Baker,* 1990], and the volume change associated with metamorphic reactions can exceed 4% (Table 3), it follows from (5) that ζ can vary significantly during metamorphism and that $\zeta \gg \eta$. Accordingly the characteristic deformation length scale for linear rheologies, δ [*McKenzie,* 1984]

(Table 1), can be approximated as

$$\delta \approx \sqrt{\frac{k}{\mu}\frac{3}{4}\frac{\eta}{\phi}}. \quad (6)$$

In compaction models, ζ is often treated as a constant parameter of the same order of magnitude as η. This is of minor importance in constraining mantle processes, but it leads to significant error in assessing the length scale of crustal deformation associated with metamorphic devolatilization.

Permeability

In combination with rheology, the permeability (i.e., the "background" permeability k_0) of the rocks about a reaction front plays a major role in determining fluid pressure evolution. As shown subsequently, the $k - \phi$ relation is of less importance, provided porosity and permeability are proportional, a reasonable supposition.

Background Permeability

Walder and Nur [1984] note that the discrepancy between the high measured permeability of crustal rocks and evidence for widespread high fluid pressure at depth can only be reconciled if permeability is a dynamic property. This permeability is constrained by metamorphic fluid fluxes [e.g., *Yardley,* 1986], for which good estimates can be made assuming that the timescale of whole crustal metamorphism is determined by heat conduction [e.g., *Norris and Henley,* 1976; *England and Thompson,* 1984]. In this case the timescale is $\tau_M \approx l_c^2/\kappa$, where l_c and κ are the crustal thickness and thermal diffusivity (Table 1). Pelite (a volatile-rich lithology) releases $\sim 84\,\mathrm{kg\,H_2O/m^3}$ rock (w_{H_2O}) in the transition from lower greenschist to granulite facies (Figure 1). This requires an average fluid flux of

$$\bar{q} \approx -\frac{l_c w_{H_2O}}{\tau_M} = -\frac{w_{H_2O}\kappa}{l_c}.$$

Although fluid pressure may fluctuate during metamorphism, phase equilibria indicate that these fluctuations must be <100 MPa (i.e., the sensitivity of petrologic barometers) and that the average fluid pressure is near lithostatic. From Darcy's law, the time-averaged permeability is then $\bar{k} = -\bar{q}\mu/(\rho_f g \Delta\rho)$. For crustal thicknesses characteristic of extensional (10 km), thermal (35 km), and collision belt metamorphism (70 km) and the parameters in Table 1, $\bar{k}$ is $\sim 10^{-20}\,\mathrm{m^2}$ ($-\bar{q} = 1 - 9 \times 10^{-9}\,\mathrm{kg\,m^{-2}\,s^{-1}}$). This is the permeability at the top of the metamorphic pile necessary to maintain lithostatic fluid pressure if devolatilization is uniform; it is thus an upper limit on k_0. More detailed, but less robust, numerical modeling of temporal and spatial variations in metamorphic fluid production [*Connolly and Thompson,* 1989; *Thompson and Connolly,* 1992] suggests k_0 may be $< 10^{-23}\,\mathrm{m^2}$. *Bickle and Baker* [1990] infer comparable metamorphic permeabilities ($10^{-22}\,\mathrm{m^2}$) and fluxes ($10^{-11}\,\mathrm{kg\,m^{-2}\,s^{-1}}$) from isotopic profiles.

Permeability-Porosity Relationships

Experiments on rocks and solid aggregates have established that above a material specific threshold porosity, typically 4–10%, permeability varies as roughly the square or cube of porosity [e.g., *Bernabe et al.,* 1982; *Bourbie and Zinsner,* 1985; *Zhang et al.,* 1994; *Lockner and Evans,* 1995]. Below this threshold porosity, the porosity exponent begins to increase rapidly, with measured values being as high as 24 [*David et al.,* 1994]. This behavior can be attributed to a progressive loss of pore connectivity [*Geugen and Dienes,* 1989] or to variations in pore shape or distribution during compaction [*Fischer and Paterson,* 1992; *Zhang et al.,* 1994; *Gavrilenko and Geugen,* 1993]. However, most $k - \phi$ measurements are done with nonsurface active fluids (e.g., argon) and at conditions where textural equilibration is unlikely. In contrast, in metamorphic systems, fluids are surface active, and fluid-solid textural equilibrium is to be expected, since equilibration in quartz aggregates occurs in a matter of hours [e.g., *Holness,* 1993]. In this case, if connectivity exists, as suggested by field evidence [e.g., *Valley and Graham,* 1991; *Chamberlain and Conrad,* 1991; *Young and Rumble,* 1993; *Skelton et al.,* 1995], it does not vary with porosity. Thus it appears reasonable to model the effect of compaction on permeability by assuming it arises from shrinkage of fully connected pipe-like hydraulic bonds. If pore structure is homogeneous, such a model leads to a quadratic dependence ($k \propto \phi^2$) [*Geugen and Dienes,* 1989], but network modeling of natural pore distributions yields a dependence that is more nearly cubic [*Zhu et al.,* 1995; cf. *Bernabe,* 1995], similar to that predicted from the Kozeny-Carman model [e.g., *Walsh and Brace,* 1984]. Accordingly, permeabilities are computed here as

$$k = \omega\phi^{n_\phi} \quad (7)$$

with $n_\phi = 3$. The proportionality constant $\omega = 10^{-13}\,\mathrm{m^2}$, is near the lower limits of the range consistent with various experiments on quartz and calcite aggregates summarized by *Zhu et al.* [1995]. The initial model porosities (ϕ_0), derived from (7) for $k_0 = 10^{-20} - 10^{-23}\,\mathrm{m^2}$, are 0.05–0.2%. The value of ω is material specific and, given existing data, varies over 4 orders of magnitude. Thus alternative parameterizations would decrease the porosity necessary to maintain k_0 by roughly a factor of 10. Such variations change ϕ_0, and this influences rheological response (equation (4)).

Governing Equations and Boundary Conditions

The rate of metamorphic dehydration is coupled to both heat and fluid flow by the dependence of ΔG on fluid pressure and temperature. Consequently, it is nec-

essary to account for both heat and fluid flow simultaneously to understand the evolution of metamorphic fluid pressure and to determine to what extent the process is thermally or mechanically controlled. Toward this end, the following governing equations are formulated to describe vertical (one-dimensional) heat and fluid flow

$$C_r \frac{dT}{dt} = K\nabla^2 T + C_f \nabla(qT) + \dot{r}_H \quad (8)$$

$$\phi\beta \frac{dp_f}{dt} + \frac{d\phi}{dt} = \frac{1}{\mu}(\nabla k(\nabla p_f - \rho_f g) + k\nabla^2 p_f) + \frac{\dot{r}}{\rho_f}. \quad (9)$$

Equation (8) equates the time rate of change in the energy per unit volume of rock with the energy gain or loss: by conduction through the rock matrix, advection by fluid movement, and enthalpic effects associated with metamorphic reactions. The coefficients in (8) are approximated well by constants (Table 1).

The conservation of fluid mass and momentum (Darcy's law) for flow of a slightly compressible fluid through a plastic matrix is described by (9). This modification of *Walder and Nur's* [1984] governing equation accounts for permeability gradients [e.g., *Gavrilenko and Geugen,* 1993] and fluid production [e.g., *Wong et al.,* 1997]. In combination with (4), (9) is a hyperbolic equation for shock waves in pressure and porosity. The left-hand terms of (9), approximate the time rate of change of fluid mass per unit volume of rock due to elastic compression, and irreversible porosity production resulting from reactions (equation (2)) and plastic deformation (equation (4)). These are equated with terms representing fluid gain by flow and fluid production by reactions. The $\beta\phi$ term approximates elastic storativity by the compressibility of the fluid. Rigorous treatment of poroelasticity introduces complexities [*Gavrilenko and Geugen,* 1993] that are unlikely to be significant if the fluid phase occupies a grain-edge network. Measured storativities differ by less than an order of magnitude from $\beta\phi$ [e.g., *Fischer and Paterson,* 1992], and this difference becomes less important in well-indurated rocks [*Palciauskas and Domenico,* 1989]. Consequently, little is gained by treatments where poroelasticity is represented by a constant, since the effect on hydraulic conductivity is negligible in comparison to the uncertainty in permeability. For these reasons, in most compaction studies, elastic effects are disregarded. The necessity of incorporating an elastic coefficient in (9) arises here because a nonisochoric reaction would otherwise generate an infinite pressure anomaly at the onset of reaction.

In the limit that deformation is insignificant, (9) reduces to a parabolic diffusion equation with a source term

$$\frac{dp_f}{dt} = \frac{k}{\mu\beta\phi}\nabla^2 p_f + \frac{\dot{r}}{\rho_f \beta\phi}. \quad (10)$$

Alternatively, if the matrix has no strength and the diffusive component of fluid flow is neglected, (9) describes porosity advection [e.g., *McKenzie,* 1984]

$$\frac{d\phi}{dt} = \frac{1}{\mu}(\omega n_\phi \phi^{n_\phi - 1}(\nabla p_f - \rho_f g))\nabla\phi + \frac{\dot{r}}{\rho_f} \quad (11)$$

where, from (7), ∇k in (9) has been replaced by $\omega n_\phi \phi^{n_\phi - 1}\nabla\phi$. A consequence of (11) is that a reaction-generated perturbation to an initially uniform porosity distribution can sharpen to, and propagate as, a shock provided the velocity of porosity advection ($\omega n_\phi \phi^{n_\phi - 1}(\nabla p_f - \rho_f g)/\mu$) is an exponentially increasing function of porosity, i.e., $n_\phi > 1$ [e.g., *Spiegelman,* 1993a]; a situation likely to be realized for geologic materials.

Equations (10) and (11) represent two extreme forms of fluid transport through the crust, pure hydraulic diffusion and deformation-propagated transport. Present analytical solutions to compaction equations [e.g., *McKenzie,* 1984; *Scott and Stevenson,* 1984; *Barcilon and Richter,* 1986; *Spiegelman,* 1993a,b] do not account for the variations in rheologic and kinetic parameters that occur in metamorphic systems. However, the relative importance of diffusion versus deformation-controlled fluid transport can be estimated from the Donut number, *Do*, the ratio of the hydraulic diffusion timescale ($\tau_D = l_c^2 \mu\beta\phi/k$) for crustal fluid transport to the timescale for changes in porosity ($\tau_C = \delta_0\mu\phi/(k\Delta\rho g)$ [*McKenzie,* 1984])

$$Do = \frac{\tau_D}{\tau_C} = l_c^2 \frac{\delta_0}{\beta}\Delta\rho g$$

where l_c is the crustal length scale. The critical variables determining the compaction length scale δ_0 (Table

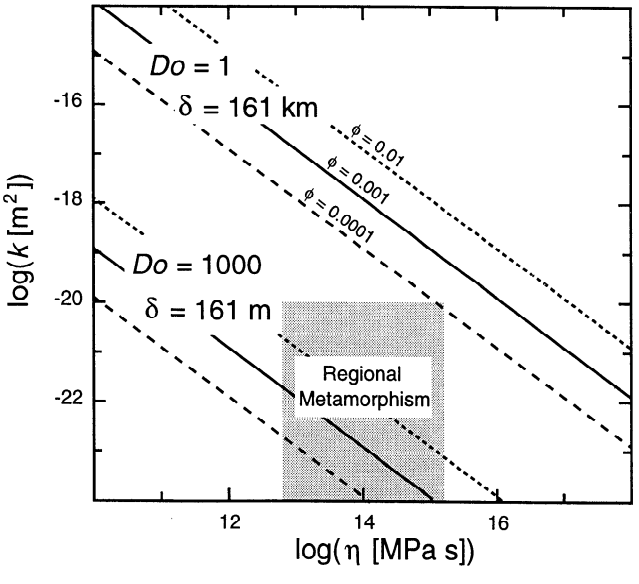

Figure 3. Ratio of the hydraulic diffusion and compaction timescales (*Do*) as a function of k, η, and ϕ for a crustal length scale $l_c = 10$ km; all other parameters as in Table 1. For the $\eta - k$ range of regional metamorphic environments (shaded), $Do > 1$ implying a significant component of metamorphic fluid transport may be propagated by deformation rather than by hydraulic diffusion.

1) are η, k_0, and ϕ_0 for the crust at the onset of reaction. For plausible ranges of these variables (Figure 3), deformation-propagated fluid flow (equation (11)) is significant ($Do > 1$).

In comparison to more rigorous treatments of compaction [e.g., *McKenzie,* 1984; *Scott and Stevenson,* 1984; *Spiegelman,* 1993ab; *Birchwood and Turcotte,* 1994] the present treatment neglects mass and momentum conservation for the rock matrix. This simplification introduces errors that scale as $1 - \phi$ in the fluid and porosity fluxes.

Fluid Pressure Boundary and Initial Conditions

The most realistic fluid pressure boundary conditions for modeling the Earth's crust are to assign high permeability and a near hydrostatic p_f gradient at the surface boundary and low permeability and a lithostatic p_f gradient at the lower boundary. Unfortunately, because a hydrostatically pressured fluid is intrinsically unstable in a deformable medium, such a configuration has no steady state solution. Preliminary calculations showed that even without metamorphic devolatilization, such boundary conditions lead to episodic flow across a lithostatic-hydrostatic transition region. While this may reflect the true nature of flow at the lithostatic-hydrostatic transition, it is an undesirable source of variability in the initial conditions for modeling. The only general steady state initial condition is obtained with uniform permeability and a lithostatic p_f gradient throughout the crust. This configuration was adopted for the models presented here and was defined by constant fluid pressure boundaries. This is unsatisfactory for describing flow in the upper crust but is a reasonable initial condition in the lower crust. The fluid pressure boundary conditions imply that in the absence of metamorphic reactions, there is a uniform fluid flux q_0 through the crust. The magnitude of the flux ($10^{-11} - 10^{-12}\,\mathrm{kg\,m^{-2}\,s^{-1}}$), and the crustal porosity (ϕ_0, 0.05–0.2%), is determined from (7) and Darcy's law for the specified background permeability ($k_0 = 10^{-21} - 10^{-23}\,\mathrm{m^2}$).

Thermal Boundary Conditions: Steady State Isograd Velocity and Fluid Flux

The initial temperature distribution is defined by a constant geothermal gradient of 30 K/km, and the initial location of the dehydration reaction front (i.e., a metamorphic isograd) is determined by the intersection of this geotherm with the equilibrium conditions ($p_f = \rho_r g z$) for the reaction of interest (Figure 4). The chief effect of varying geothermal gradients is rheological and thus is simulated by varying crustal strength. Thermal metamorphism is induced by changing the temperature at the lower crustal boundary ($z = 25$ km), while holding the surface boundary temperature constant (273 K). The rate of temperature change at the lower boundary is chosen so that if the geotherm were to remain linear

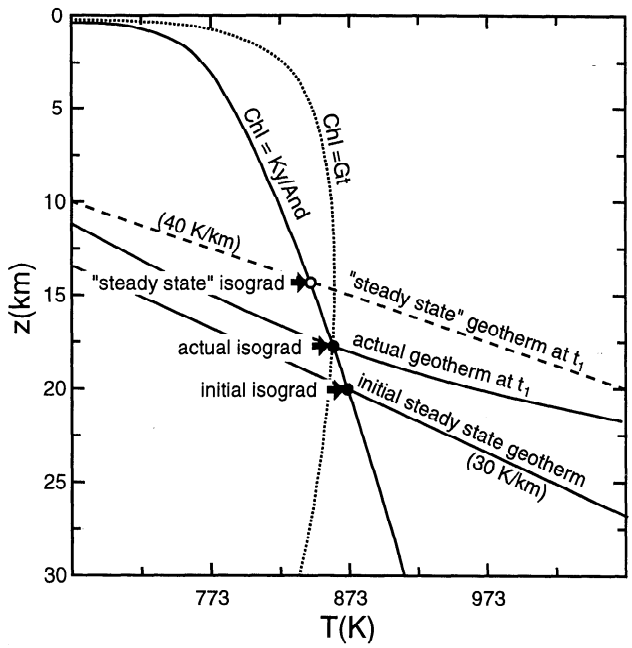

Figure 4. Initial ($p_f = \rho_r g z$) $T - z$ coordinates of the Chl ⇒ Ky and Chl ⇒ Gt equilibria (Table 3). The initial depth of the reaction front (isograd) is determined by the intersection of the geotherm (30 K/km) with the relevant equilibrium boundary. During metamorphism, the equilibrium $T - z$ coordinates vary with fluid pressure. Metamorphic heating rate is specified by the steady state vertical isograd velocity (v_{ss}), for example, the upward velocity of the intersection of the geotherm and the equilibrium reaction boundary of interest in the absence of thermal or mechanical effects. The true isograd lags behind this intersection but may move with velocity approaching v_{ss} if the reaction rate is thermally controlled.

(i.e., in the absence of any thermal effects) the intersection of geotherm with the equilibrium boundary would advance upward at a constant velocity, referred to hereafter as the steady state isograd velocity (v_{ss}, Figure 4). Because of finite heat conduction rates, the true isograd position lags behind this hypothetical steady state isograd. However, in the limit that reaction kinetics become thermally controlled rather than determined by fluid pressure or chemical kinetics, the isograd velocity approaches v_{ss}. In this case, if the fluid is expelled instantaneously, the steady state fluid flux in excess of q_0 is $q_{ss} = w_{H_2O} v_{ss}$. The steady state isograd velocity is roughly equivalent to the rate of advance of an isotherm through the crust during metamorphism. Field studies [e.g., *Rubie,* 1986; *Thompson,* 1989; *Vance,* 1995] and thermal models [e.g., *England and Thompson,* 1984; *Connolly and Thompson,* 1989] indicate that isotherm velocities of $\sim -1 \times 10^2 - 10^3$ m/Myr are characteristic of regional metamorphic environments. Rates at the lower and higher ends of this range are associated with collision belt and extensional regimes, respectively. For these rates, and parameters in Table 2, $-q_{ss} = 1.1 \times (10^{-10} - 10^{-9})\,\mathrm{kg\,m^{-2}\,s^{-1}}$. These fluxes

would require permeabilities 0 – 2 orders of magnitude, and porosities almost 1 order of magnitude, larger than the background values.

Model Synopsis

The model assumptions and structure can be summarized as follows: (1) The amount, rate, and conditions for fluid release are a function of fluid pressure and temperature from equation (2). (2) Total porosity production is that due to creep in response to nonzero effective pressure (equation (4)) combined with porosity produced through reduction in solid volume by chemical reactions ($\dot{r}\Delta V_s$). (3) Permeability is proportional to the cube of porosity (equation (7)). Initial permeability and porosity are taken to be uniform throughout the crust. (4) With the exceptions of porosity, permeability, f_{H_2O}, and, in the case of nonlinear rheologies, shear viscosity, all fluid and matrix properties are treated as constants (Table 1). (5) The velocity of the rock matrix is neglected. (6) The initial fluid pressure distribution is lithostatic and maintained by a steady fluid flux. The initial geothermal gradient is 30 K/km. (7) Heat and fluid flow is orthogonal to Earth's surface. (8) Metamorphic heating is simulated by raising the temperature at the base of the crust ($z = 25$ km) as a variable function of time (at rates of 4–50 K/Myr). (9) The evolution of fluid pressure and temperature is evaluated by simultaneous solution (Appendix B) of equations (2), (4), (8), and (9).

Model Results: Linear Rheology

In this section, a specific model calculation is considered first to illustrate some general characteristics and implications of reaction-generated fluid flow. Variations on this model are used subsequently to assess the influence of the character of the devolatilization reaction, deformation style (microcracking), and changes in more fundamental parameters (i.e., v_{ss}, ϕ_0, k_0, and η).

Fluid Pressure-Porosity Evolution: Constant Shear Viscosity, Chl ⇒ Ky Reaction

The $p_f - \phi$ evolution for the Chl ⇒ Ky dehydration with moderate rock strength, low permeability and rapid heating rate is shown in Figure 5 (model 1, Table 5). This configuration leads to a simulation that approaches the isochoric-closed system end-member scenario for metamorphism. In this scenario a reaction that induces an isobaric $\Delta V > 0$ must lead to overpressuring and, in terms of the Mohr-Coulomb criterion, weakening and possibly embrittlement. This occurs at the onset of reaction ($t < 0.5$ Myr, Figure 5a) when a small positive p_f anomaly is coincident with the reaction front. However, the anomaly is < 20 MPa, possibly too small to cause brittle failure in light of measured tensile strength of silicate rocks [e.g., *Geugen and Palciauskas,* 1994; cf. *Dutrow and Norton,* 1995]. With increas-

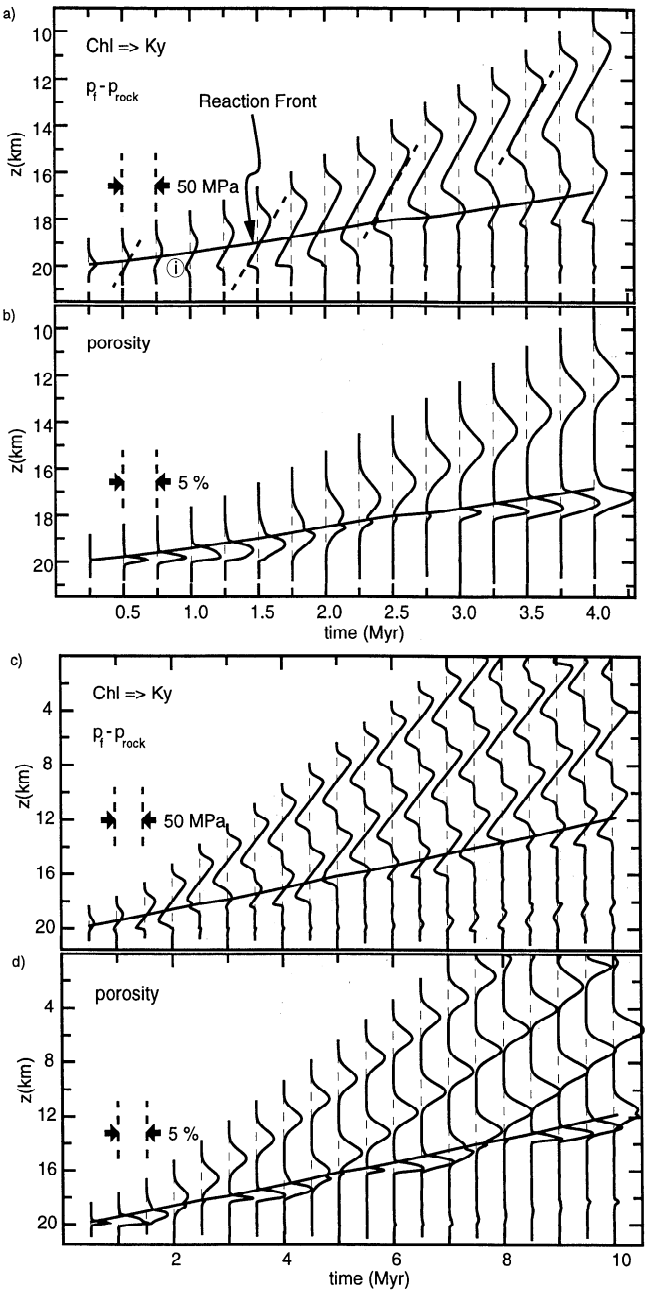

Figure 5. The $p_f - \phi$ evolution for Chl ⇒ Ky ($\Delta V > 0$) dehydration with $v_{ss} = 1000$ m/Myr, $\eta = 10^{14}$ MPa s, $k_0 = 10^{-22}$ m^2. (a) Fluid pressure anomaly ($p_f - \rho_r g z = -p_e$) and (b) porosity as a function of depth and time. Dashed base lines represent lithostatic pressure in Figure 5a or zero porosity in Figure 5b. Spacing between adjacent profiles corresponds to a fluid pressure anomaly of 50 MPa (Figure 5a) or 5% porosity (Figure 5b). Position of the reaction front (uppermost extent) is indicated by the subhorizontal curve crossing the profiles. In Figure 5a diagonal dashed lines indicate hydrostatic p_f gradient. (c) and (d) The $p_f - \phi$ evolution for the same model over a longer time span. Maximum width of the reaction zone is 110 m at ~1 Myr; thereafter the width decreases linearly with time, dropping to 60 m by 10 Myr. The reduction in width is related to increasing obliquity of the equilibrium $p - T$ conditions to the geotherm.

Table 5. Characteristics of ϕ Waves for Various Model Configurations

Model	k_0, m^2	η, MPa s	ϕ_0, %	v_{ss}, km/Myr	δ_0, km	λ_ϕ, km	λ_p, km	ϕ_1, %	$\bar{\phi}$, %	v, km/Myr	R	U	$\nabla p_f - \rho_f g$, MPa/km	$-p_e$, MPa	Ra
1	10^{-23}	10^{14}	0.046	1	0.13	1.4	2.9	3.4	1.7	3.2	0.2	0.4	0.088	25	0.3
2	10^{-22}	10^{14}	0.1	1	0.27	2.1	3.0	1.0	0.68	6.2	0.6	0.07	2.0	19	0.04
3	10^{-23}	10^{14}	0.046	0.1	0.13	0.89	1.2	0.25	0.19	0.99	2.3	0.04	5.3	6.4	0.0007
4	10^{-23}	10^{14}	0.1	1	0.09	1.1	2.5	20	8.5	1.9	0.1	0.7	0.016	22	0.6
5	10^{-22}	10^{15}	0.1	1	0.87	6.6	10.1	0.20	0.18	7.0	0.8	0.07	1.9	72.7	0.8
6	10^{-22}	10^{15}	0.1	0.1	0.87	6.0	5.4	0.11	0.074	1.5	1.7	0.01	15	9.9	0.01
7	10^{-21}	10^{14}	0.2	1	0.59	5.7	3.5	0.42	0.39	12.6	0.7	0.02	16	48	0.03
8	10^{-22}	10^{13}	0.1	1	0.09	0.54	0.86	0.68	0.50	5.9	3.2	0.07	3.8	5.2	0.003
9	10^{-23}	10^{14}	0.046	1	0.13	1.7	2.6	0.48	0.31	4.2	0.9	0.4	0.058	23.2	0.4
10	10^{-21}	PL3	0.2	1	-	0.2-2	1-5	2-3	0.9-1.3	-	-	-	0.1-0.2	6-60	0.01-0.5
11	10^{-23}	PL3	0.046	0.1	-	0.2-2	1-5	0.7-5	0.4-2	<1.3	-	-	0.003-0.2	7-55	0.04-0.2
12	10^{-21}	PL4	0.2	1	-	0.4-3	2-6	3-6	2-3	-	-	-	0.1-0.2	17-62	0.08-0.8
13	10^{-23}	PL4	0.046	0.1	-	0.4-3	2-6	3-6	1.6-1.7	-	-	-	0.004-0.1	24-75	0.3-1.8
14	10^{-23}	10^{14}	0.046	1	0.13	1.4	2.9	3.3	1.7	3.2	0.2	0.4	0.090	25	0.3

See Figure 9. All models are for the Chl ⇒ Ky reaction (Table 3) with $n_\phi = 3$, with the exceptions of model 9 for which $n_\phi = 5$, and model 14 for the Chl ⇒ Gt reaction (with $n_\phi = 3$). For model 4, $\omega = 10^{-13}\,m^2$; for model 9, $\omega = 10^{-6.33}\,m^2$; and for all other models $\omega = 10^{-13}\,m^2$. The maximum amplitude of the porosity anomaly is ϕ_1, and the wavelength λ_ϕ is the full width of the anomaly at $\phi = (\phi_1 - \phi_0)/2$. The pressure anomaly wavelength λ_p is the distance between inflections in p_e with depth, $\bar{\phi}$ is the average porosity over this interval, and $-p_e$ is the p_f anomaly at the upper inflection point. $\nabla p_f - \rho_f g$ is the difference between the actual and hydrostatic p_f gradients at the wave midpoint; the average value of $\nabla p_f - \rho_f g$ is $2p_e/\lambda_p$. With nonlinear rheologies (models 10–13, Table 4) the evolution of ϕ waves, and fluid movement, is controlled by interactions between waves, and wave characteristics vary strongly with time.

ing time, hydraulic diffusion causes the p_f anomaly to propagate roughly symmetrically away from the reaction front and, in turn, causes dilational deformation (porosity inflation) above and below the reaction front (0.5 Myr, Figure 5b). Within this region of deformation the increase in permeability permits fluid to flow more rapidly than it can pass through the obstruction represented by the undeformed rocks. Consequently, the p_f gradient in the deformed region must relax toward a hydrostatic limit, a limit that is nearly realized (Figure 5 and Table 5). The first manifestation of relaxation is the upward displacement of the maximum in the p_f anomaly above the reaction front. This displacement amplifies the p_f anomaly, because of the divergence of fluid pressure from lithostatic conditions, which in turn increases the rate of pore dilation above the reaction front. This feedback mechanism creates a mechanical instability that grows larger with time until the rate of dilational strain in the rocks above the reaction front exceeds volumetric fluid production, whereupon fluid pressure at the reaction front begins to decrease, the rocks below become underpressured, and a negative p_f anomaly develops (Figure 5a, 1.0 Myr, point i). Compaction drives the negative anomaly upward and ultimately beyond the reaction front so that the permeable, high-porosity region becomes isolated from the fluid source, producing a shock wave of anomalous fluid pressure, porosity, and fluid flux (2.75 Myr, Figure 5a). For a matrix with constant shear viscosity, pore compaction is the mirror image of dilation. Thus once the positive and negative fluid pressure anomalies are isolated from the fluid source, they become symmetric, propagate with constant velocity and form, and the mean fluid pressure within the wave is identical to the mean confining pressure. Such waves correspond to deformation-propagated fluid flow, which is a component of the overall fluid flow provided deformation has an increasing nonlinear effect on permeability, i.e., $n_\phi > 1$ (equation (9), [e.g., *Spiegelman,* 1993a]). An implication of this behavior is that the largest p_f anomaly, i.e., lowest effective pressure, occurs above, rather than coincident with, the dehydration reaction front. Drainage and compaction of the rocks below the reaction front create an obstruction to upward fluid flow, initiating a train of diminishing porosity waves below the reaction front. This behavior is not pronounced in the present example but is evident in other simulations (Table 5) and provides a mechanism by which deformation can be propagated downward against the direction of fluid and porosity flow [*Spiegelman,* 1993b].

Kinetic controls. The time-integrated and short-term average (0.1 Myr interval) reaction rates (integrated over the width of the reaction front), normalized to the steady state reaction rate ($v_{ss} w_{H_2O}$), are plotted as a function of time in Figure 6. At the onset of reaction, these rates lag considerably behind the steady state rate due to the retarding effects of increased fluid pressure and chemical kinetics. With time, the integrated rate approaches the steady state, indicating that the rates are ultimately controlled by the rate of heat

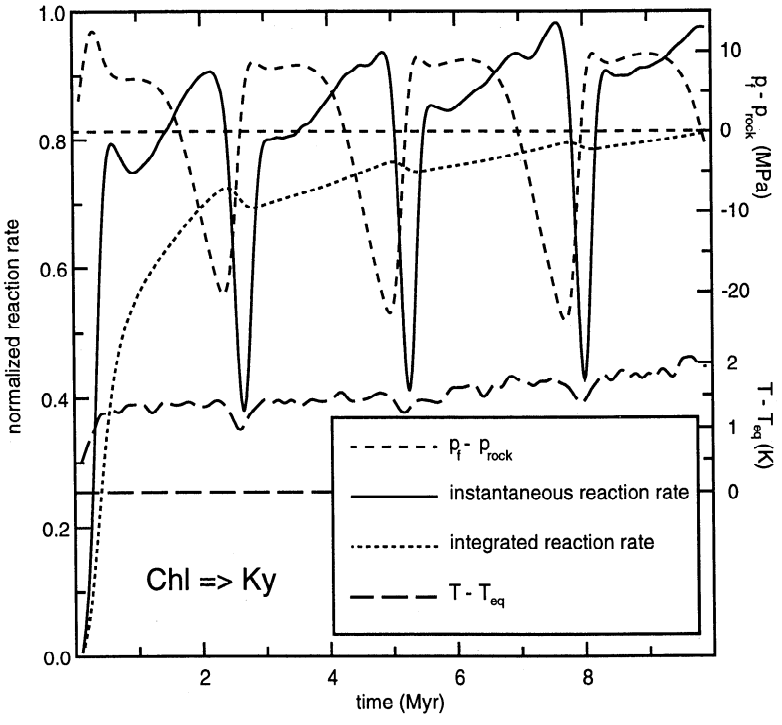

Figure 6. Reaction rates (scale on left axis), p_f anomaly ($p_f - p_{rock}$, dashed curve), and difference between the actual and equilibrium temperature at the reaction front (scales on right axis) for Chl $\Rightarrow$ Ky dehydration (Figure 5) as a function of time. Integrated ($\int(\int \dot{r}dz)dt$) and short-term ($\int \dot{r}dz$ averaged over 0.1 Myr intervals) reaction rates are normalized to the thermally controlled steady state rate (1.1×10^{-7} kg H_2O m^{-2} s^{-1}). Because of the inverse relation between $\dot{r}$ and p_f, most reaction occurs while the effective pressure is high and the rock is relatively strong. High heating rates used for this calculation maximize the importance of chemical kinetics, yet the degree of disequilibrium as measured by the temperature overstep is unimportant. Overall reaction rates are essentially equilibrium rates dictated by the rate of heat input and modulated by fluid pressure variations.

input. This result is not surprising given the small magnitude of the reaction enthalpy in comparison to the thermal inertia of crustal metamorphism. However, fluid pressure oscillations at the reaction front must affect reaction rate and are therefore inconsistent with the existence of a true steady state as illustrated by oscillations in the short-term average rate (Figure 6). The general form of these oscillations is easily understood. At the onset of the reaction the increase in fluid pressure acts to raise the equilibrium temperature, increasing ΔG for the reaction and thereby quenching it. Once fluid pressure begins to decrease, as deformation above the reaction front permits fluid to drain, reaction rates increase (Figure 6). Consequently, the amount of reaction that occurs while the rocks are potentially brittle is small in comparison to that which takes place while the reaction front is underpressured and strong. Even for the high heating rates implicit in this model, chemical kinetics does not play a significant role. This is reflected by the small temperature overstep above the equilibrium dehydration temperature required (Figure 6) for the reaction to keep pace with the variations in temperature and fluid pressure caused by thermal and mechanical processes.

Fluxes and thermal and mass consequences of episodic flow. Although the concentration of fluid into pulses associated with porosity waves cannot affect the time-integrated fluid flux above a reaction front, it can magnify the instantaneous fluxes. From the separation of the porosity waves (Figure 5d), it can be estimated that the average flux within the waves is roughly twice that necessary to accommodate that generated by dehydration ($\int \dot{r}dz = 0.7 \times 10^{-9}$ kg m^{-2} s^{-1}, Figure 6). Fluxes vary locally within a wave such that in the central portions, fluxes may exceed the steady state fluxes by an order of magnitude. Magnification of instantaneous fluxes is due not only to the focusing of flow into pulses but also to more efficient crustal drainage by pulsed flow in comparison to steady flow.

Because the efficacy of advective transport by fluid flow is determined by instantaneous flux rates [e.g., *Bickle and McKenzie,* 1987], such temporal focusing may enhance forced heat and mass advection. To assess this, the model temperature evolution is compared to that computed for pervasive steady state fluid flow (Figure 7). This comparison shows that the advective heat effect associated with fluid pulses produces temperature anomalies of <10 K, and perturbs the local geothermal

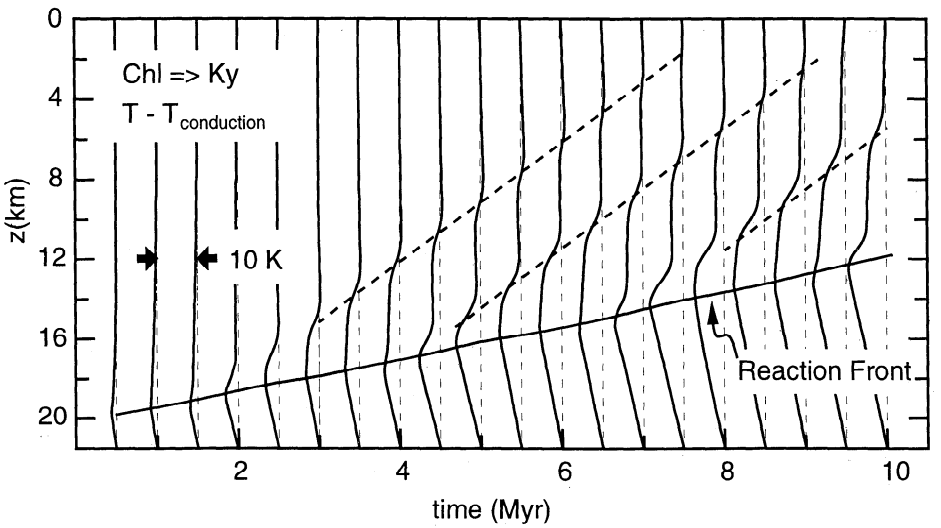

Figure 7. Advective and enthalpic heat effects for the Chl ⇒ Ky dehydration model, as shown in Figure 5, as a function of time and depth in the crust. Each profile shows the difference between the temperature for the complete model and that obtained (T_{cond}) when enthalpic and advective effects are not included. The largest effect (~ -10 K) is associated with the reaction front and due to endothermic dehydration. Three additional perturbations to the geotherm can be identified (dashed lines) that correspond to advection of heat by pulsed fluid flow. These increase the geothermal gradient within the porosity wave, by ~ 10 K/km, and thereby increase the efficacy of mass transport. The advective heat anomaly must vanish toward the surface due to the isothermal boundary condition.

gradient by <10 K/km. For the model conditions this perturbation roughly doubles the silica solubility gradient (-8×10^{-6} kg SiO_2/kg H_2O/m [*Manning,* 1994]), and therefore the silica mass transport that would occur in silica-saturated rocks. Were reaction to continue for 10 Myr this process would precipitate ~1 vol % quartz in the effected rocks, a potential mechanism for quartz-vein formation. This result is linearly dependent on the rate of metamorphic devolatilization, which may well be an order of magnitude lower in natural systems.

Fluid mixing and convection. The fluid in the unperturbed matrix moves with velocity $v_0 = q_0/\phi_0\rho_f$; thus in a reference frame that moves with a porosity wave, the porosity within the wave experiences a volumetric fluid flux of $(v_0 - v)\phi_0$, where v is the velocity of the wave. Consequently, fluid and porosity travel together only in the limit that $\phi_0 \to 0$ or $v_0 \to v$. In the time required for the wave to reach the surface (v/l_c), the ratio (R) of the integrated external flux to the total amount of fluid per unit area within the wave ($\approx \lambda_p\bar{\phi}$) is

$$R = \frac{(v_0/v - 1)\phi_0 l_c}{\lambda_p \bar{\phi}}. \qquad (12)$$

If the wave travels $l_c \approx 20$ km, $R = 20\%$, the high porosities obtained for this simulation minimizes this effect. Values of R in excess of 300% are obtained for alternative model configurations (Table 5). This type of mixing has been suggested as a mechanism of removing the chemical signature of the fluid source from the fluid within a porosity wave [*Scott and Stevenson,* 1986; *Spiegelman,* 1993a].

A hydrostatic p_f gradient, such as nearly exists within porosity waves, is a necessary condition for free convection of pore fluids. For the model configuration, free convection occurs for modified Rayleigh numbers

$$Ra' = \frac{g\beta_T\rho_f\nabla T\omega\phi^{n_\phi}\lambda_p^2}{\kappa\mu} > 4\pi^2 \qquad (13)$$

where λ_p is the wavelength of the pressure wave and β_T is the thermal expansivity of the fluid [*Bear and Bachmat,* 1991]. Taking average properties for the porosity waves (model 1, Table 5), $Ra' = 0.3 \ll 4\pi^2$, it may be concluded that free convection does not occur. Parameter variations, discussed below, lead to conditions that are comparable, or less favorable, for free convection.

The Role of ΔV, Chl ⇒ Gt Reaction

The $p_f - \phi$ evolution (Figures 8a and 8b) for the Chl ⇒ Gt reaction (model 14, Table 5), with $\Delta V < 0$, is remarkably similar to that for the Chl ⇒ Ky ($\Delta V > 0$) reaction. The most significant difference being that at the onset of reaction the rocks are strengthened by underpressuring ($t < 0.75$ Myr, Figure 8a). However, as the reaction front advances, it leaves a region of high porosity and permeability in its wake in which the p_f gradient must approach hydrostatic conditions. Eventually, compaction, particularly at the base of this region, raises fluid pressure at the reaction front above the confining pressure, initiating positive dilational strain. Once this occurs, fluid pressure variations are determined primarily by deformation rather than the prop-

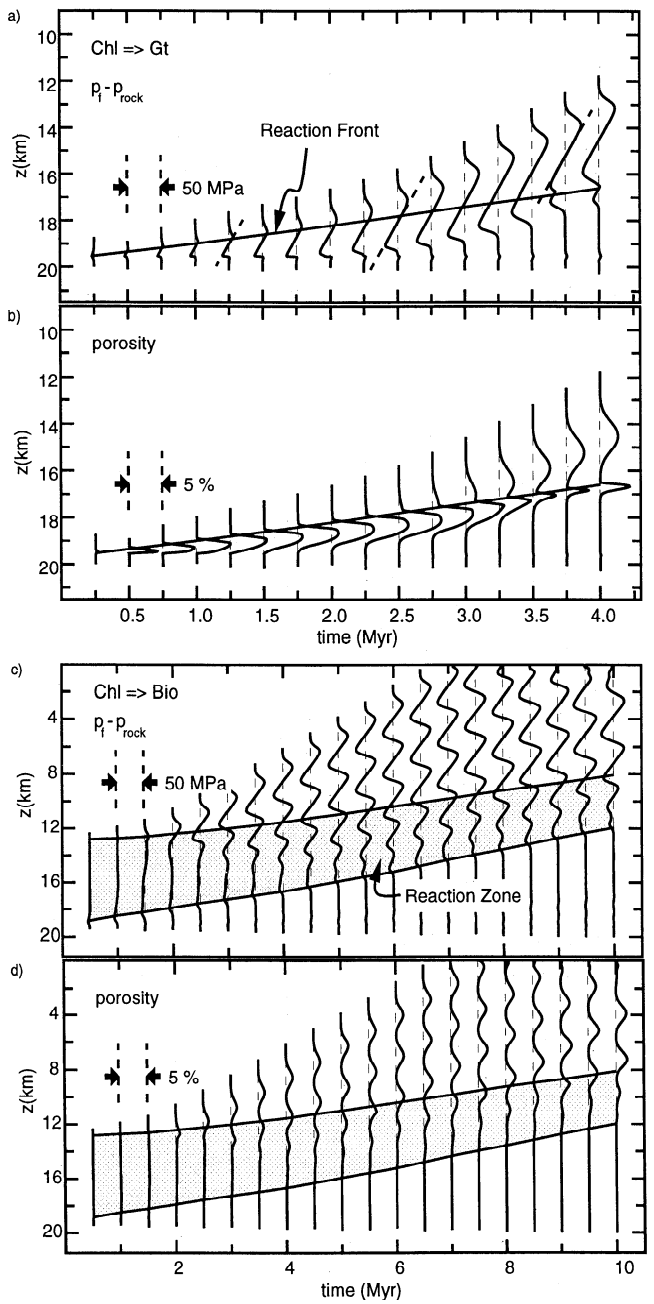

Figure 8. (a) Fluid pressure and (b) porosity evolution for Chl ⇒ Gt dehydration ($\Delta V < 0$). (c) Fluid pressure and (d) porosity evolution for continuous Chl ⇒ Bio ($\Delta V = 0$) dehydration. Both models computed with $v_{ss} = 1000\,\mathrm{m/Myr}$, $\eta = 10^{14}$ MPa s, and $k_0 = 10^{-22}\,\mathrm{m}^2$.

erties of the reaction, and the $p_f - \phi$ evolution of the system is identical to that of $\Delta V > 0$ reaction. However, in contrast to $\Delta V > 0$ reactions, increasing fluid pressure increases the rate of fluid production so the greatest amount of reaction occurs while the rocks are weakest. This has the counterintuitive implication that a $\Delta V < 0$ reaction is at least as a $\Delta V > 0$ reaction to generate hydrofracturing in spatial association with the reaction front.

Continuous Dehydration and $\Delta V > 0$ Reactions

Continuous Chl ⇒ Bio dehydration results in similar behavior (Figures 8c and 8d) to the discontinuous dehydration reactions. This reflects the fact that any reaction, irrespective of its ΔV, creates a domain of increased permeability. Because the overlying rocks obstruct the flow of fluid from this domain, the p_f gradient relaxes within this permeable region initiating mechanical instability that ultimately generates a porosity wave. Thus any perturbation the fluid flux of an initial steady-flow regime results in a component of deformation propagated flow, and the specific distribution of the fluid source (e.g., due to lithologic heterogeneity) is a secondary factor.

Microcracking

Microcracks induced by reaction-generated fluid overpressure can affect fluid flow in two ways. Experimental evidence suggests that extraordinary reaction rates may be necessary to for reaction-induced microcracking to affect connectivity and enhance permeability [*Connolly et al.*, 1997]. In the limit of this behavior, the effect of microcracking is rheological rather than hydraulic and can be simulated by a reduction in rock strength as considered in the subsequent section. Alternatively, if the degree of microcrack connectivity varies, n_ϕ (equation (7)) would increase as permeability drops toward the percolation threshold [*Geugen and Dienes*, 1989]. This is simulated by a constant, but increased, porosity exponent ($n_\phi = 5$) in model 9 (Figure 9 and Table 5). The simulation shows that an increase in the porosity exponent decreases the amplitude and increases the velocity of the high-porosity domains. Thus fluid flow remains episodic, but the total flux associated with each pulse is reduced. As discussed below, rheologic softening counters this, but without a more detailed model of the influence of microcracks on permeability and rheology, the net effect cannot be quantified.

The implications of larger-scale hydrofracture are similar to those of microcracks, the key issue being the degree of connectivity. Measured in situ fracture permeabilities [e.g., *Brace*, 1984] are vastly in excess of those necessary to accommodate metamorphic fluid production; thus it appears unlikely that there is fracture connectivity on a crustal scale. Nonetheless, domains of connected fractures might provide a mechanism of deformation-propagated flow [*Gold and Soter*, 1985].

Parameter Variation and Wave Trains

There are four major model variables, background permeability k_0, shear viscosity η, reaction rate as related to the steady state isograd velocity v_{ss}, and the $k-\phi$ relationship (Figure 9 and Table 5). Aside from the variation in wave properties that these induce, the most notable feature of simulations with parameter choices alternative to those discussed earlier (Figure 9 and Ta-

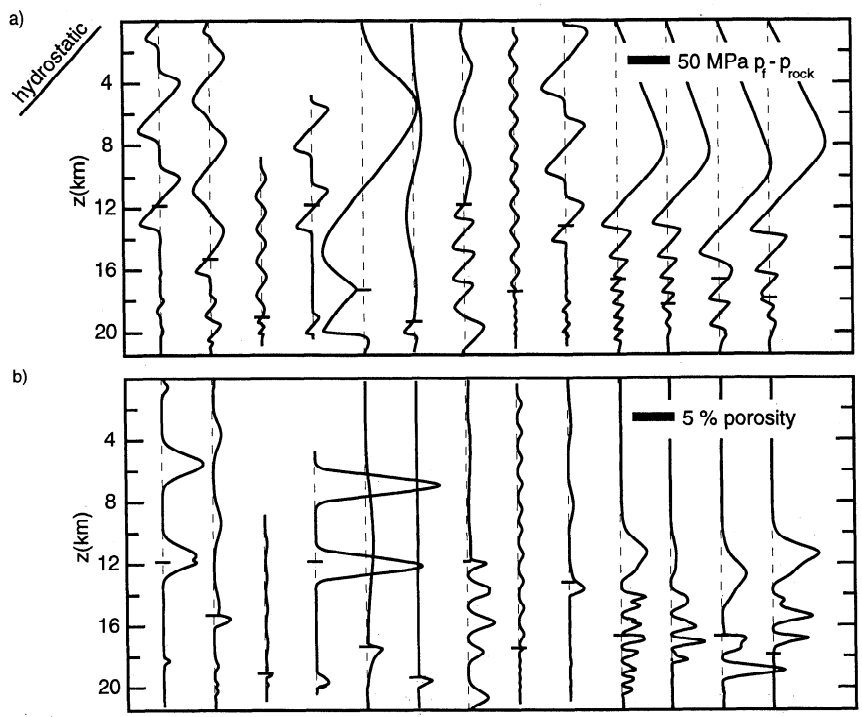

model	1	2	3	4	5	6	7	8	9	10	11	12	13
t(Myr)	10	6	10	10	3.5	6.5	10	4	8.5	4.5	18	4.5	20/50
log(k[m^2])	-23	-22	-23	-23	-22	-22	-21	-22	-23	-21	-23	-21	-23
log(η [MPa s])	14	14	14	14	15	15	14	13	14	PL3	PL3	PL4	PL4
ϕ (%)	0.05	0.1	0.05	0.1	0.1	0.1	0.2	0.1	0.05	0.2	0.05	0.2	0.05
v_{ss} (km/Myr)	1	1	0.1	1	1	0.1	1	1	1	1	0.1	1	0.1

Figure 9. Effects of parameter variations on (a) p_f and (b) ϕ evolution for Chl ⇒ Ky dehydration; for additional information see Table 5. All models were computed with $n_\phi = 3$ (equation (7)), with the exception of model 9 for which $n_\phi = 5$. In each profile the reaction front position is indicated by a horizontal line. In model 13, metamorphic heating was terminated at 20 Myr, but deformation and fluid flow were permitted for an additional 30 Myr.

ble 5) is the formation of porosity wave trains. This results because, prior to wave detachment, the high-porosity domain above the reaction front continues to grow until the volumetric fluid flux into the domain is identical to the background flux above the domain (q_0/ρ_f). Once this occurs, the domain detaches from the reaction front as a porosity wave. After detachment, the wave is isolated from its source and, barring variations in the fundamental properties of the fluid or matrix, propagates with unchanging form. It follows that porosity waves cannot initiate unless they conduct the fluid flux generated by the reaction. Since the average flux generated by the reaction, in the thermally controlled limit, is q_{ss}, this condition can be expressed as $v\Delta\phi \geq q_{ss}/\rho_f$, where $\Delta\phi = \phi_1 - \phi_0$ is the wave amplitude, and in the limit $v\Delta\phi \rightarrow q_{ss}/\rho_f$ the waves form a wave train with nodes at ϕ_0 [*Scott and Stevenson,* 1984].

Wavelength. An increase in either k_0 (model 4⇒5) or rock strength (i.e., η/ϕ_0, models 2⇒8 and 4⇒1) allows fluid to flow farther from the reaction front in a given time interval causing more diffuse deformation and increasing the wavelength of porosity waves. This relationship of k_0 and rock strength to wavelength is embodied in the characteristic length scale for deformation, δ (Table 1, [*McKenzie,* 1984]). The wavelength, λ_ϕ, of porosity waves is, within a factor of 2, proportional to, and an order of magnitude greater than, the compaction length of the unperturbed matrix δ_0 (Figure 10a and Table 5).

The compaction length characteristic of regional metamorphic environments may vary from 10 to 10000 m (Figure 3), provided linear rheologies maintain in the crust. The maximum p_f anomaly associated with a porosity wave is proportional its wavelength (i.e., $\lambda/2\rho_f g$). This suggests two limiting scenarios that are, for petrologic purposes, indistinguishable from steady flow. At large δ_0, deformation and fluid pressure variations would be diffuse. At low δ_0, flow would be accomplished by a continuum of small waves with small associated fluid pressure variation (<4 MPa). In contrast, for intermediate δ_0 of 100–1000 m, fluid flow is

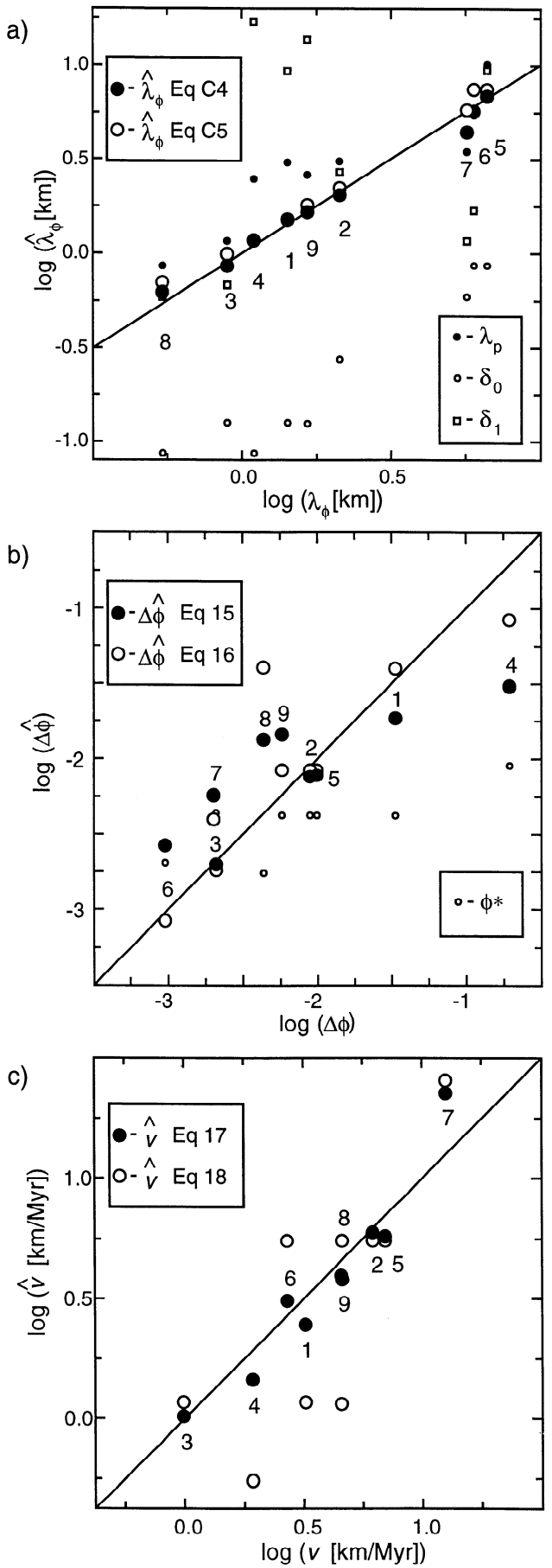

discretized on a small enough scale to be observable in a geologic context, yet fluid pressure variations may be comparable to the rock tensile strength.

If the crust strengthens upward, the compaction length of the unperturbed rock matrix also increases upward. In such an environment a porosity wave becomes more attenuated as it propagates, i.e., increases its wavelength at the expense of porosity. In general, it can be expected that attenuation does not significantly affect the fluid pressure gradient (see discussion below), so that this process magnifies the fluid pressure anomalies associated with a porosity wave and may activate other deformation mechanisms such as hydrofracture.

Amplitude. The total porosity production above the midpoint of a porosity wave ($z = z_1$) can be approximated as (Appendix C)

$$\dot{V} = -(\phi_1 + \phi_0)\lambda_\phi^2(\nabla p_f - \rho_r g)\frac{4}{3}\frac{c_0}{\eta}, \qquad (14)$$

where $c_0 = 0.144$ is an integration constant and $\nabla p_f - \rho_r g$ is the effective pressure gradient. A porosity wave will begin to detach from a reaction front when the fluid flux across the midpoint of the wave, $q_1 = -\dot{V} + q_0$, exceeds the fluid flux immediately above the reaction front, $\approx q_{ss} + q_0$. Equating these fluxes and solving for $\Delta\phi$ yields an estimator for porosity wave amplitude

$$\Delta\hat{\phi} \geq \frac{3q_{ss}\eta}{4c_0\lambda_\phi^2(\nabla p_f - \rho_r g)} - 2\phi_0. \qquad (15)$$

From Darcy's law, for the fluid pressure gradient above the reaction front to remain lithostatic, the porosity must be $\phi^* = (-(q_{ss}+q_0)\mu/(\omega\rho_f\Delta\rho g))^{1/n_\phi}$. The piezometric gradient, $\nabla p_f - \rho_f g$, necessary to drive the flux $q_{ss} + q_0$ varies as ϕ^{n_ϕ}; thus for $\phi_1 > \phi^*$ the piezometric gradient drops exponentially toward hydrostatic conditions (Table 5). Therefore, in the limit of large porosity waves, $\phi_1 \gg \phi^* > \phi_0$, the gradient in the effective pressure, $\nabla p_f - \rho_r g$, that is responsible for the deformation within the wave approaches $-\Delta\rho g$. Making this approximation and assuming that λ_ϕ can be expressed as a linear function of δ_0, i.e., $\lambda_\phi \approx \alpha\delta_0$, then

$$\lambda_\phi^2 \approx \alpha^2\frac{k_0}{\mu}\frac{3}{4}\frac{\eta}{\phi_0},$$

and (15) simplifies to

$$\Delta\hat{\phi} \geq \frac{q_{ss}}{c_0\alpha^2 v_0\rho_f}, \qquad (16)$$

Figure 10. Comparison of porosity wave (a) wavelength, (b) amplitude, and (c) velocity with various estimators for the constant linear rheology models (Figure 9 and Table 5).

where $\alpha = 7.8$ from regression of the results of simulations 1–9 (Table 5). In the simulations, the reaction-generated fluid fluxes only approach q_{ss} as a limiting value, and the linear relationship between λ_ϕ and δ_0 is only accurate within a factor of 2. Given this, the success of (16) in estimating a lower bound on wave amplitude is remarkable (Figure 10b). The rationale for (15) and (16) is that porosity waves detach from the reaction front when q_1 approaches q_{ss}, but if the wave propagates relatively slowly, the amount of deformation that occurs after this condition is reached may be substantial. Such circumstances lead to well-separated waves with substantially larger amplitudes than predicted from (16) (e.g., models 1 and 5, Table 5). Equations (15) and (16) also do not take into account the role of fluid pressure in modulating the rate of fluid production at the reaction front; however, the similarity of the porosity waves generated by the Chl ⇒ Gt and Chl ⇒ Ky models (models 1 and 14, Table 5 and Figures 5 and 8) suggests that coupling of reaction rate to fluid pressure has little influence on wave amplitude.

Velocity and conditions for propagation. For a porosity wave to propagate with unchanging form, $\dot{V}$ (equation (14)) must be identical to the porosity flux across the wave midpoint, $v\Delta\phi$. Equating these quantities and solving for v yields an estimator for the porosity wave velocity

$$\hat{v} = \frac{1}{\Delta\phi}\left(-(\phi_1 + \phi_0)\lambda_\phi^2(\nabla p_f - \rho_r g)\frac{4}{3}\frac{c_0}{\eta}\right) \qquad (17)$$

or in the limit of large porosity waves, as discussed above

$$\hat{v} = c_0\alpha^2 v_0. \qquad (18)$$

Velocities computed with (18) are in broad agreement with those of the numeric simulations (Figure 10b). This implies that wave velocity is determined in large part by the initial velocity of the fluid in the unperturbed matrix, and, for the range of parameters considered here, is largely independent of the physical properties of the matrix or fluid. Velocities deviate from this behavior as $\phi_1 \rightarrow \phi_0$ (e.g., models 6 and 7 where $\phi_1/\phi_0 \approx 2$), whereupon velocity varies as the inverse of wave amplitude (equation (17)). Since the amplitude of a porosity wave cannot exceed unity, (16) and (18) imply that for wave propagation to occur,

$$\phi_0\frac{q_{ss}}{q_0} = U < c_0\alpha^2, \qquad (19)$$

where $c_0\alpha^2 \approx 10$. As $U \rightarrow c_0\alpha^2$ the separation of the waves increases (Table 5 and Figure 9) until the high-porosity domain becomes confined ($v - v_{ss} \rightarrow 0$) by the reaction front. Thereafter, the porosity can only propagate beyond the front after fluid production ceases. This behavior occurs in numeric simulations with $U \approx 1$, slightly greater than the value for model 4 (Table 5).

Model Results: Nonlinear Rheology and Crustal Heterogeneity

Model results are shown in Figure 11 for the weakest of the three experimentally determined quartzite rheologies (PL3, Table 4). Nonlinear rheologies enhance deformation propagated fluid transport because nonlinearity magnifies the instability of perturbations to the lithostatic p_f gradient. Thus wave phenomena are important in models with power law rheologies over a wider parameter range (Table 5), most notably for k_0, than for linear models. Power law behavior causes the dilational strain rate to rise rapidly away from the midpoint of a wave, this produces a uniform porosity distribution and p_f gradients that are nearly hydrostatic (Table 5 and Figure 9). These conditions are more favorable for free convection within individual waves than those attained in linear models, but Ra numbers (equation (13)) are well below the critical value.

The effective viscosity, and therefore the compaction length, of a power law rheology becomes infinite as the flow stress goes to zero; consequently, the initial perturbation generated by devolatilization for such a rheology develops with long wavelength. The obstruction to flow created by compaction at the base of this perturbation causes the subsequent porosity wave to develop with shorter wavelength and higher amplitude. In this respect the similarity of the Newtonian and power law models is illusory. In Newtonian models, wave trains form by propagation of waves away from the reaction front, whereas in power law models wave trains result because, with time, successive waves initiate closer to the reaction front. Indeed, with strong power law rheologies (PL4 and GT4, Tables 4 and 5 and Figure 9) or high reaction rates (Figures 11c and 11d) the propagation of individual waves is insignificant.

These phenomena reflect not only the variable length scales that arise through the effect of compaction on the matrix porosity but also the increasing strength of the rheologies with falling temperature. Increase in rock strength causes porosity waves to slow as they propagate upward; this acts to increase the associated p_f anomalies. It can be argued that the extreme p_f anomalies generated must inevitably lead to hydrofracture, at least in the upper crust. However, hydrofracturing must accelerate fluid drainage above the obstruction formed by compaction at the base of a porosity wave, and this accelerates compaction and increases the tendency of waves to form at greater depth.

Upward slowing of porosity waves due to crustal strengthening permits later waves to interact with those formed earlier. This is illustrated in Figure 11b, commencing at 10 Myr when wave 1, not yet isolated from the reaction front, begins to impinge on the superjacent wave 2. The increased fluid flow into wave 2 isolates wave 1 from the reaction front by 11 Myr. Fluid is then drained from the upper portion of wave 2, until at 12 Myr it becomes isolated from wave 1 as well. Once

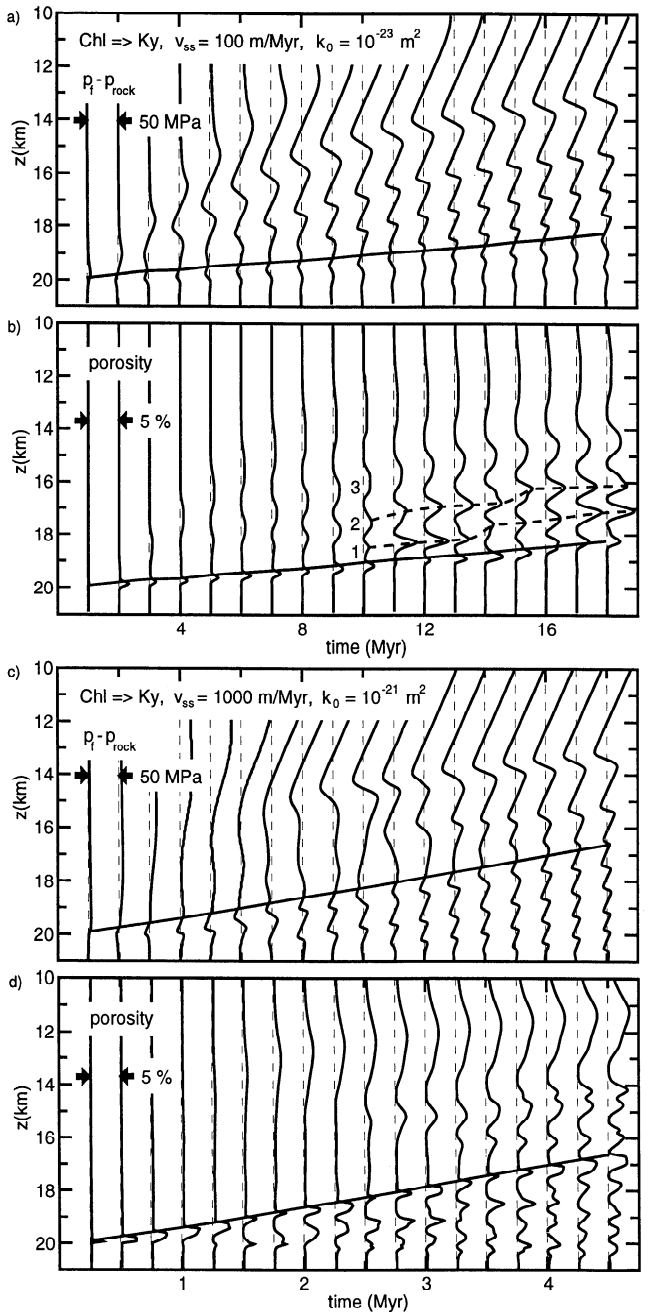

Figure 11. The $p_f - \phi$ evolution for Chl $\Rightarrow$ Ky dehydration with *Paterson and Luan's* [1990] quartzite power law creep rheology (PL3, Figure 2 and Table 4). (a) Fluid pressure and (b) porosity profiles computed with $v_{ss} = 100$ m/Myr and $k_0 = 10^{-23}$ m^2. (c) Fluid pressure and (d) porosity profiles computed with $v_{ss} = 1000$ m/Myr and $k_0 = 10^{-21}$ m^2.

isolated, the resulting bimodal porosity distribution in wave 1 is unstable, and the porosity maximum shifts rapidly upward until the porosity distribution reaches a quasi-equilibrium state at 15 Myr. The influx of fluid into wave 2 initiates a similar instability which culminates in the upward propagation of the porosity maximum of wave 2 between 14 and 15 Myr and the achievement of new quasi-equilibrated porosity distribution by 16 Myr. The overall effect of this process is that fluid is transported upward more rapidly than the waves propagate through the interaction of adjacent waves and that the propagation of individual waves occurs in discrete episodes associated with instabilities induced by fluid flux or rheologic changes.

If a more efficient deformation mechanism, such as hydrofracture or pressure solution, does not begin to operate, then at some point the uppermost wave reaches depths where deformation becomes insignificant. After this occurs, the porosity of the wave continues to increase as fluid is transferred from lower waves and compaction reduces the wavelength of the stationary wave. In the absence of deviatoric stresses, this would increase the mechanical stability of the system and provide a positive feedback mechanism favoring the formation of high-porosity water "sills" [*Fyfe et al.*, 1978]. Such sills would have effectively no strength and therefore would be unstable under deviatoric stress.

Model 13 (Figure 9 and Table 5) demonstrates that extraordinary timescales (>50 Myr) would be required to form a sill in a rheologically continuous medium, but a similar effect results from introducing heterogeneity in a simulation (Figure 12). Here the heterogeneity is an order of magnitude stronger, 100 m thick layer 3000 m above the reaction front. This layer causes the porosity waves to stall at considerably greater depth than in the homogeneous model. Once this occurs, dilation

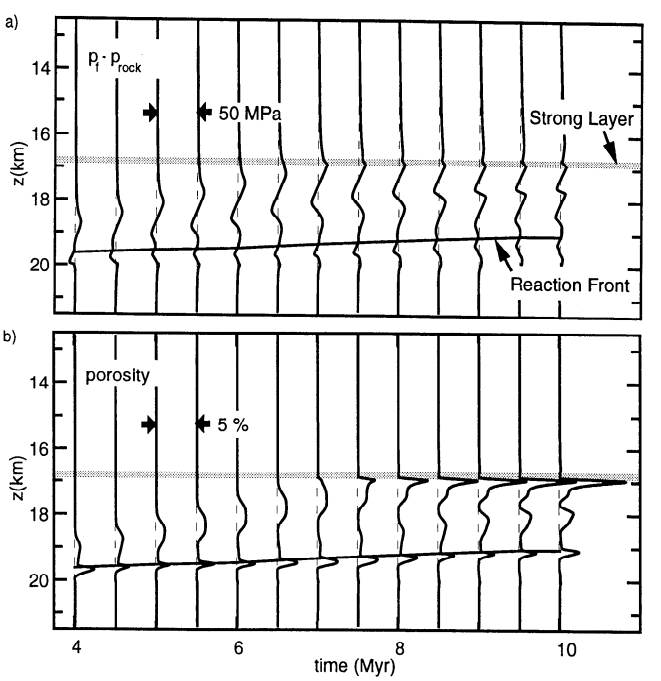

Figure 12. Effect of heterogeneity on $p_f - \phi$ evolution for Chl $\Rightarrow$ Ky dehydration with $v_{ss} = 100$ m/Myr, $k_0 = 10^{-22}$ m^2, and *Paterson and Luan's* [1990] quartzite power law creep rheology (PL3, Figure 2, Table 4). The location of the heterogeneity, which is 20 times stronger than the surrounding rocks, is indicated by shading. Fluid does not pond beneath the heterogeneity if the strength contrast is reduced to a factor of 10.

of the porosity immediately beneath the layer reduces the vertical extent of the wave. The consequent reduction in rock strength and p_f anomaly within the water "sill" has a positive feedback on this process in that it increases the relative strength of the overlying rock and lessens the hydraulic head driving fluid flow. Similar behavior results from heterogeneity in any material property that substantially slows the propagation of porosity waves but depends on both the magnitude and scale of heterogeneity. In nature it can be expected that such phenomena would lead to the fluid flow paths that exploit [e.g., *Yardley and Lloyd,* 1995], or create [*Wiggins and Spiegelman,* 1995], lateral heterogeneities.

Summary and Discussion

Thermodynamic stability of volatile-bearing metamorphic mineralogies and high compaction rates of underpressured porosity in silicate rocks provide compelling arguments that fluid pressure must approach lithostatic values during metamorphism. Given regional metamorphic timescales and volatile budgets, this requires time-averaged crustal permeabilities to be $< 10^{-20}\,m^2$. However, permeabilities approaching 10^{-16} m^2 are necessary to drain fluid from discontinuous metamorphic reaction fronts. This inconsistency can only be reconciled if fluid production is accommodated in porosity generated by the reaction and by local deformation. Numerical simulation of this process shows that a $\Delta V < 0$ reaction leaves a region of underpressured high porosity and permeability in its wake. Because fluid flow in this region is restricted by relatively impermeable rocks above the reaction front, fluid pressure relaxes toward a hydrostatic gradient. Divergence of the p_f gradient from the lithostat causes compaction by creep at depth and eventually raises fluid pressure at the reaction front causing dilational deformation. Once this occurs, the positive p_f anomaly drives fluid flow into the overlying rocks, generating dilational strain, i.e., porosity, in these rocks, while compaction collapses porosity at depth. The net effect of this is to propagate the high-porosity domain beyond the reaction front. As long as this region of enhanced permeability is in contact with the reaction front, it must continue to grow, causing the fluid pressure anomalies at the upper and lower extremes to become larger with time. Ultimately, the dilational strain rate at the top of the high-porosity domain exceeds volumetric fluid production by the reaction and compaction isolates the porosity domain from the reaction front. Thereafter, the domain of fluid-filled porosity propagates as a wave of anomalous porosity and fluid pressure. The only significant difference in this behavior for a $\Delta V > 0$ reaction is that at the onset of reaction the porosity is overpressured, so the high-porosity domain develops primarily above the reaction front. Virtually any process that perturbs a steady state hydrologic regime, e.g., continuous devolatilization, must cause some form of deformation-propagated fluid flow. Comparison of timescales for hydraulic diffusion and compaction by plastic deformation suggests that for plausible metamorphic permeabilities, deformation-propagated fluid flow is likely to be a significant transport mechanism on crustal length scales.

Implications for Rock Strength

The volume change of metamorphic reactions has been ascribed considerable importance for rock mechanics. It being thought that $\Delta V > 0$ reactions generate fluid overpressuring and embrittlement, whereas $\Delta V < 0$ result in underpressuring and strengthening. This study suggests that this zero-dimensional model is an oversimplification in that, for either case, fluid pressure oscillates about the lithostat due to compaction processes. Indeed, kinetics of $\Delta V < 0$ reactions are enhanced by high fluid pressure, thus such reactions produce more fluid while the reaction front is weak. The primary factors leading to embrittlement during dehydration are the connected porosity generated by the reduction in solid volume; the divergence of fluid and rock pressure gradients within this porosity; and compaction. The magnitude of ΔV is a secondary factor influencing only the timing of embrittlement. Whether or not embrittlement actually occurs and its implication for fluid flow is uncertain. The small overpressures (<50 MPa) required to permit deformation-propagated fluid flow by creep suggest that embrittlement is not inevitable. The notion that metamorphic rocks are not only subject to supralithostatic fluid pressure but can withstand overpressures approaching 100 MPa without embrittlement is supported by field evidence [e.g., *Simpson,* 1997]. If embrittlement does occur, it weakens the rheology and causes stronger dependence of permeability on porosity. Both these effects enhance the wave-like character of fluid flow and reduce the fluid pressure anomalies associated with devolatilization. In this respect, the models provide a best case scenario for the situation that must precede the development of self-propagating fluid-filled fractures [e.g., *Nakashima,* 1995; *Walther and Orville,* 1982]. At low temperatures or extraordinary reaction rates (such as characteristic of contact metamorphism), plastic deformation may become negligible, in which case, deformation must be either elastic or brittle. The evolution of fluid pressure under these circumstances is discussed by *Hanson* [1995], *Dutrow and Norton* [1995], and *Wong et al.* [1997].

Characteristics of Porosity Waves and Middle to Lower Crustal Metamorphic Fluid Flow

That pulsed flow is an almost inescapable feature of melt flow through a deformable matrix is well established [e.g., *Scott and Stevenson,* 1984; *Barcilon and Richter,* 1986]. This work details the scale and importance of this phenomenon in metamorphic environ-

ments. For Newtonian rheologies and the parameter ranges likely in such environments, to a first approximation the characteristics of porosity waves are such that wavelength is proportional to the compaction length of the unperturbed rock matrix, velocity is determined by the velocity of the fluid through the rock matrix at the onset of reaction, v_0, and amplitude is proportional to the ratio of the reaction-generated fluid flux, q_{ss}, to v_0. Wave frequency is inversely proportional to the dimensionless quantity $U = \phi_0 q_{ss}/q_0$, where ϕ_0 and q_0 are the porosity and fluid flux at the onset of reaction. This proportionality implies large perturbations to metamorphic fluid flow regimes generate large isolated porosity waves. However, wave-propagated fluid flow patterns vary from being highly episodic to essentially indistinguishable from steady flow. In the latter case, flow is accomplished by high-frequency, low-porosity waves with small associated fluid pressure anomalies. This type of behavior provides a possible explanation for the numerous crack-seal cycles observed in some metamorphic quartz veins [e.g., *Fisher and Brantley,* 1992]. Nonlinear (power law) rheologies magnify the mechanical instabilities generated by metamorphic reactions with the result that large amplitude porosity waves develop over a wider parameter range.

Multidimensional effects. Since the work of *Norton and Knight* [1977] the relative importance of buoyancy versus pressure-driven flow has been debated in metamorphic petrology. Near-hydrostatic fluid pressure gradients are a requirement for buoyancy-driven flow; but compaction is too efficient for this condition to be characteristic of the midcrust and lowercrust in general. However, the pressure gradient necessary to drive fluid flow within porosity waves can be negligibly greater than hydrostatic, particularly in large amplitude waves. Despite this, the characteristics of the waves are such that free convection is unlikely, implying that middle to lower crustal fluid flow is pressure driven. Under these circumstances, and in the absence of external forcings [e.g., *Sibson,* 1987], fluid flow must always have an upward deformation-propagated component. The importance of this component in determining the overall characteristics of flow will depend on the relative magnitude of the lateral flux components that develop in response to lateral variations in permeability, such as those created by fracture zones or folding, or fluid production rates. The distance scales over which such variations may influence flow are constrained by the one-dimensional models presented here in that compaction rates become comparable to metamorphic fluid production rates at effective pressures of ~10 MPa. Large lateral pressure gradients would thus cause porosity to collapse and isolate the metamorphic fluid source.

In a homogeneous porous medium, two- and three-dimensional instabilities are known to cause one-dimensional porosity waves to become channeled into cylindrical or spherical waves [*Stevenson,* 1989; *Wiggins and Spiegelman,* 1995]. In melt transport, heat advection provides a positive feedback mechanism that promotes wave channelization, but in metamorphic systems, heat advection is minor and quartz precipitation may mitigate against channelization [*Connolly,* 1996]. Further, in natural systems anisotropic permeability due to variations in structure and lithology are almost certainly more important factors in controlling flow and the geometry of high-porosity domains. In any event, multidimensional effects can only accelerate the compaction process. The one-dimensional models employed here thus provide conservative estimates for the drainage of metamorphic fluids. In preliminary work, *Wiggins and Spiegelman* [1995] show that, in a homogenous three-dimensional matrix, spherical waves have diameters and spacing of $\sim 16\delta_0$ and propagate at velocities slightly greater than, but comparable to, the original one-dimensional waves. Three-dimensional wave phenomena on this scale would result in roughly a fourfold increase in instantaneous fluid fluxes over those computed for one-dimensional models. Given the uncertainties in model parameters, an effect of this magnitude does not significantly alter conclusions drawn from the one-dimensional models.

Crustal heterogeneity. Provided fluid production rates have a net tendency to increase with depth during metamorphism, the details of fluid production, and thus the lithological homogeneity of the crust, are unimportant for the development of porosity waves. However, rheological heterogeneity introduces a variety of complexities in the dynamics of porosity wave propagation. Two types of rheological heterogeneity have been considered: continuous upward strengthening of the crust and discontinuous variation in strength due to lithologic heterogeneity. Upward strengthening causes porosity waves to slow and lengthen as they propagate upward. Because the p_f anomaly driving the deformation is proportional to the length of the porosity wave, this increases the p_f anomaly and ultimately must cause embrittlement. Heterogeneities that impede upward propagation of a wave without affecting the compaction rate at the base of the high-porosity domain have the opposite effect in that they result in reduction of the p_f anomaly. If this effect is large enough, it can cause porosity waves to become trapped beneath the obstruction thus forming high-porosity sills. In the absence of deviatoric stress, the mechanical stability of such a sill would increase with time, but low shear strength would make such sills unstable under deviatoric stress. Model calculations show that an order of magnitude increase in rock strength is sufficient to cause sill formation. Numerical simulation of heterogeneous permeability is precluded here by the requirement of steady initial conditions, but it can be anticipated from *McKenzie's* [1984] dimensional analysis that an order of magnitude reduction in permeability would have the same effect. Since order of magnitude variations in permeability and strength are likely throughout the crust, in nature, fluid flow may

be accomplished by the ponding of pervasive flow beneath relatively impermeable or strong lithologic units, i.e., aquitards. In such a scenario, flow would occur periodically, and catastrophically, if the aquitards were breached by fracturing induced by far field stresses.

Advection effects. It is generally agreed that pervasive regional metamorphic fluid fluxes are too small to effect significant advective transport and that metamorphic fluid flow must be focused if this is to occur [e.g., *Brady,* 1989; *Peacock,* 1989; *Connolly and Thompson,* 1989]. However, geometric models of focused flow require extraordinary degrees of lateral fluid flow [*Brady,* 1989; *Chamberlain and Rumble,* 1989; *Connolly,* 1996]. Temporal focusing of fluid flow that results from the concentration of fluid into pulses associated with porosity waves, is also a mechanism capable of enhancing regional metamorphic fluid fluxes. The resulting advective transport generates local thermal anomalies of <10 K, and increases the amount of silica transported by less than a factor of 2. More impressive advective transport may result from a combination of geometric and temporal focusing, but multidimensional modeling is necessary to assess the feasibility of this.

Kinetic Controls on Devolatilization

The initial goal of this study was to understand the coupling of reaction, deformation, and flow rates during metamorphism through the dependence of these rates on fluid pressure. Since devolatilization reactions must perturb the metamorphic hydrologic regime in which they occur, the classical petrological model of devolatilization as an isobaric, thermally controlled process is a limiting case that cannot be realized. The other limiting case is that represented by an isochoric model, where the rate of reaction is controlled by drainage, i.e., mechanical control. The numeric simulations suggest that on average devolatilization is thermally controlled but that on the timescale of that required to generate a porosity wave, reaction rates are modulated by fluid pressure variations. This modulation is sympathetic to, but not necessary for, the formation of porosity waves, which develop even if reaction rates are independent of fluid pressure (i.e., $\Delta V = 0$). Thus mechanical control of reaction kinetics has little influence on devolatilization or deformation for heating rates characteristic of regional metamorphism. Chemical kinetic controls modify this behavior only in determining the displacement of physicochemical conditions from those of thermodynamic equilibrium necessary for thermal or mechanical processes to become rate limiting [e.g., *Ridley,* 1986]. Chemically limited kinetic rates are uncertain, but for the rate laws applied here based on muscovite dehydration [*Schramke et al.,* 1987; *Lasaga,* 1986], the thermal overstepping for this is small (<3 K).

Appendix A: Chemical Kinetic Model

Reaction rates are estimated here after the nonlinear kinetic model of *Lasaga* [1986], who assumed that the rate limiting factor is the surface area of one mineral. By analogy with the experimental study of *Schramke et al.* [1987] that established that aluminosilicate was the rate limiting mineral for muscovite dehydration, kyanite and garnet are considered to be the rate limiting minerals for the Chl ⇒ Ky and Chl ⇒ Gt reactions. To make this analogy quantitative, a molar unit of the rate limiting mineral is defined on the basis of a five oxygen formula unit. The bulk rate of reaction ($\mathrm{kg\,H_2O/m^3}$ rock/s) is

$$\dot{r} = Mc|\Delta G|^{n_r} A_{\mathrm{RLM}} \tag{A1}$$

where $M = \nu_{\mathrm{H_2O}} \mathrm{N_{H_2O}}/\nu_{\mathrm{RLM}}$ (Table 3), A_{RLM} is the surface area of the rate limiting mineral per unit volume rock, n_r is a constant expected to vary between 2.6 and 2.9 [*Lasaga,* 1986], and c is the rate constant. The temperature dependence of the rate constant is estimated from the Arrhenius expression [*Lasaga and Rye,* 1993]

$$c = c_0 \exp\left[-\frac{E}{\mathrm{R}}\left(\frac{1}{T} - \frac{1}{T_0}\right)\right] \tag{A2}$$

where c_0 is the rate constant at the reference temperature T_0 and E is the activation energy. Parameters for (A1) and (A2) were taken from *Lasaga* [1986] ($n_r = 2.68$, $c_0 = 4.4 \times 10^{-18}\,\mathrm{mol\,H_2O\,m^{-2}\,s^{-1}}$, $T_0 = 874\,\mathrm{K}$) and *Schramke et al.* [1987] ($E = 189\,\mathrm{kJ/mol\,H_2O}$).

Nucleation and the variation of mineral surface area as a function of reaction progress are complex phenomena. To avoid treating these phenomena, the surface area $A_{\mathrm{RLM}} = 201\,\mathrm{m^{-1}}$ is taken as a constant. This value is obtained when the mode of the rate limiting mineral is 3 vol % (roughly one half the modes indicated in Table 3), and the mineral grains are spherical with a radius of 0.44 mm. Computations with more complex models in which A_{RLM} was computed as a function of reaction progress and in which grain size aspect ratios were allowed to vary, show that these factors have minor influence on the overall model results.

Appendix B: Numerical Solutions

Equations (8) and (9) were solved iteratively by a second-order accurate Crank-Nicolson finite difference scheme with upwind differencing used for gradients. In any time step, rates from (2) and (4) were estimated using the average of the past and future potentials (p_f and/or T), with the estimate of the future values being refined iteratively until they converged within a specified tolerance ($\delta p_f < 10^{-4}$ MPa and $\delta T < 10^{-5}$ K).

For the parameter ranges considered, stable numeric solutions of (9) are difficult to obtain by standard difference techniques because of strong spatial variations in fluid fluxes and high Courant numbers. To circumvent this difficulty, an adaptive grid generation technique [*Thompson,* 1984] was used in which the density of the nodal points used for discretization was proportional to $|\nabla p_f - \rho_f g|$. A variable time step was specified such that the maximum change in fluid pressure in any

time step was <0.01 MPa. Precision of the numeric solutions was evaluated by continuously monitoring fluid mass balance. In all solutions presented, the maximum error in transported fluid mass was <0.1% of the total fluid involved; however, errors as large as 25% occur in the computation of the amount of fluid released at the reaction front. Numerical results were found to be insensitive to variations by a factor of 2 in the time step or number of nodes employed (1000 for most reported calculations).

Appendix C: Geometric Model for Porosity Waves

Within the resolution of the constant η numeric models, porosity waves are symmetric and well described by a Gaussian function,

$$\phi = \phi_0 + \Delta\phi 16^{(-(z-z_1)^2/\lambda_\phi^2)}. \quad \text{(C1)}$$

From (4), the integrated porosity production rate above the wave midpoint at z_1 is

$$\dot{V} = \int_{z_1}^{z_1+l} \frac{(\nabla p_f - \rho_r g)\phi}{\eta} dz, \quad \text{(C2)}$$

where l is the distance above z_1 at which porosity falls to ϕ_0 and $\nabla p_f - \rho_r g$ is the gradient of the effective pressure. ∇p_f is approximately linear over λ_p and falls rapidly toward zero for $z > z_1 + \lambda_p/2$ (Figure 9). Since $\lambda_p \approx 3/2\ \lambda_\phi$ (Table 5), it is reasonable to suppose that the bulk of the porosity production occurs in the region where $\nabla p_f - \rho_r g$ is approximately constant; in this case substituting (C1) into (C2) yields

$$\dot{V} = -(\phi_1 + \phi_0)\lambda_\phi^2(\nabla p_f - \rho_r g)\frac{4}{3}\frac{c_0}{\eta}, \quad \text{(C3)}$$

where $c_0 = 0.144$ is an integration constant (for $l = 0.76\ \lambda_\phi$). The accuracy of (C3) can be tested by equating $\dot{V}$ to the volumetric fluid flux in excess of q_0 across z_1, $-k_1/\mu(\nabla p_f - \rho_f g) - q_0/\rho_f$, to obtain an estimator for λ_ϕ

$$\hat{\lambda}_\phi = \sqrt{-\frac{\zeta_1\zeta_0}{c_0(\zeta_1+\zeta_0)}\frac{k(\nabla p_f - \rho_f g)/\mu + q_0/\rho_f}{\nabla p_f - \rho_r g}}. \quad \text{(C4)}$$

If the fluid flux within a wave is $\gg q_0$ and $\phi_0 \ll \phi_1$, (C4) simplifies to

$$\hat{\lambda}_\phi = \delta_1\sqrt{-\frac{1}{c_0}\frac{\nabla p_f - \rho_f g}{\nabla p_f - \rho_r g}}. \quad \text{(C5)}$$

Wavelengths from (C5), using amplitudes and fluid pressure gradients computed for the full model (Table 5), agree with those of the full model (Figure 10a), which suggests that the approximations made in obtaining (C3) are reasonable.

Acknowledgments. I am grateful to Yuri Podladchikov, who explained to me whatever I understand about nonlinear waves. The presentation and science of this paper were improved through official reviews by an anonymous reviewer, Doug Rumble, and Bill Durham and by informal reviews by John Ridley, Dave Olgaard, Jiba Ganguly, Bruce Yardley and Rainer Abart. Discussions with Marian Holness, Guy Simpson, Suz-chung Ko, Teng-fong Wong, Lisa Dell'Angelo, and Mike Bickle corrected many of my misconceptions and Max Schmid and Stefano Poli corrected my english. Computational facilities were provided by Thomas Driesner. This work was supported by Swiss National Science Foundation grant 21-36503.93.

References

Ashby, M.F., The modeling of hot isostatic pressing, *Proceedings HIP: Hot Isostatic Pressing - Theories and Applications*, edited by T. Garvare, pp. 29-40, Centek, Lulea, Sweden, 1988.

Barcilon, V., and F.M. Richter, Non-linear waves in compacting media, *J. Fluid. Mech., 164*, 429-448, 1986.

Bear, J., and Y. Bachmat, *Introduction to Modeling of Transport Phenomena in Porous Media*, 553 pp., Kluwer Acad., Norwell, Mass., 1991.

Beere, W.A., A unifying theory of the stability of the stability of penetrating liquid phases and sintering pores, *Acta Metall., 23*, 131-138, 1975.

Bernabe, Y., The transport properties of cracks and pores, *J. Geophys. Res., 100*, 4231-4241, 1995.

Bernabe Y., W.F. Brace, and B. Evans, Permeability, porosity and pore geometry of hot pressed calcite, *. Mech. Mater., 1*, 173-183, 1982

Bickle, M.J., and J. Baker, Advective-diffusive transport of isotopic fronts: An example from Naxos, Greece, *Earth Planet. Sci. Lett. 97*, 78-93, 1990.

Bickle, M.J., and D. McKenzie, The transport of heat and matter by fluids during metamorphism, *Contrib. Mineral. Petrol., 95*, 384-392, 1987.

Birchwood, R.A., and D.L. Turcotte, A unified approach to geopressuring, low-permeability zone formation, and secondary porosity generation in sedimentary basins, *J. Geophys. Res., 99*, 20051-20058, 1994.

Bourbie, T., and B. Zinsner, Hydraulic and acoustic properties as a function of porosity in Fontainebleau Sandstone, *J. Geophys. Res., 90*, 11524-11532, 1985.

Brace, W.F., Permeability of crystalline rocks: New in situ measurements, *J. Geophys. Res., 89*, 4327-4330, 1984.

Brace, W.F., and D.L. Kohlstedt, Limits on lithospheric stress imposed by laboratory experiments, *J. Geophys. Res., 85*, 6348-6252, 1980.

Brady, J., The role of volatiles in the thermal history of metamorphic terranes, *J. Petrol., 29*, 1187-1213, 1989.

Bredehoft, J.D., and H.B. Handshaw, On the maintenance of anomalous fluid pressures, I, Thick sedimentary sequences, *Geol. Soc. Am. Bull., 79*, 1097-1106, 1968.

Bruton, C.J., and H.C. Helgeson, Calculation of the chemical and thermodynamic consequences of differences between fluid and geostatic pressure in hydrothermal systems, *Am. J. Sci., 283A*, 540-588, 1983.

Chamberlain, C.P., and M.E. Conrad, Oxygen zoning in garnet, *Science, 254*, 403-406, 1991.

Chamberlain, C.P., and D. Rumble, The influence of fluids on the thermal history of a metamorphic terrain: New Hampshire, USA, *Evolution of Metamorphic Belts*, edited by J.S. Daly, R.A. Cliff, and B.W.D. Yardley, *Geol. Soc. Spec. Publ., 43*, 203-213, 1989.

Connolly, J.A.D., Calculation of multivariable phase dia-

grams: An algorithm based on generalized thermodynamics, *Am. J. Sci., 290*, 666-718, 1990.

Connolly, J.A.D., Mid-crustal focused fluid movement: Thermal consequences and silica transport, *Fluid Flow and Transport in Rocks*, edited by B. Jamtveit, B.W.D. Yardley, pp. 235-250, Chapman and Hall, New York, 1996.

Connolly, J.A.D., and B. Cesare, C – O – H – S fluid composition and oxygen fugacity in graphitic metapelites, *J. Metamorph. Geol., 11*, 379-388, 1993.

Connolly, J.A.D., and A.B. Thompson, Fluid and enthalpy production during regional metamorphism, *Contrib. Mineral. Petrol., 102*, 346-366, 1989.

Connolly, J.A.D., I. Memmi, V. Trommsdorff, M. Franchi-eschelli, and C.A. Ricci, Forward modeling of calcsilicate microinclusions and fluid evolution in a graphitic metapelite (NE Sardinia), *Am. Mineral., 79*, 960-970, 1994.

Connolly, J.A.D., M.B. Holness, D.C. Rubie, and T. Rushmer, Reaction-induced microcracking: An experimental investigation of a mechanism for anatectic melt extraction, *Geology*, in press, 1997.

Dahlen, F.A., Metamorphism of nonhydrostatically stressed rocks, *Am. J. Sci., 292*, 184-198, 1992.

David, C., T.-f. Wong, W. Zhu, and J. Zhang, Laboratory measurements of compaction induced permeability change in porous rocks: implications for the generation and maintenance of pore pressure excess in the crust, *Pure Appl. Geophys., 143*, 425-456, 1994.

Dutrow, B., and D. Norton, Evolution of fluid pressure and fracture propagation during contact metamorphism, *J. Metamorph. Geol., 13*, 677-686, 1995.

England, P.C., and A.B. Thompson, Pressure-temperature-time paths of regional metamorphism, I, Heat transfer during the evolution of regions of thickened crust, *J. Petrol., 25*, 894-928, 1984.

Etheridge, M.A., V.A. Wall, and R.H. Vernon, The role of the fluid phase during regional metamorphism and deformation, *J. Metamorph. Geol., 1*, 205-226, 1983.

Ferry, J.M., Metamorphic hydrology at 13 km depth and 400-550 C, *Am. Mineral., 72*, 39-58, 1987.

Fischer, G.J., and M.S. Paterson, Measurement of permeability and storage capacity in rocks during deformation at high temperature and pressure, in *Fault Mechanics and Transport Properties of Rocks*, edited by B. Evans, T.-f. Wong, pp. 213-252, Academic, San Diego, Calif., 1992.

Fisher, D.M., and S.L. Brantley, Models of quartz overgrowth and vein formation: deformation and episodic fluid flow in an ancient subduction zone, *J. Geophys. Res., 97* 20043-20061, 1992.

Fyfe, W.S., N.J. Price, and A.B. Thompson, *Fluids in the Earth's Crust*, 333 pp., Elsevier, New York, 1978.

Ganguly, J., *Energetics of Geological Processes*, 266 pp., Springer-Verlag, New York, 1977.

Gavrilenko, P., and Y. Geugen, Fluid overpressures and pressure solution in the crust, *Tectonophysics, 21*, 91-110, 1993.

Geugen, Y., and J.K. Dienes, Transport properties of rocks from statistics and percolation, *Math. Geol., 21*; 1-13, 1989.

Geugen, Y., and V.V. Palciauskas, *Introduction to the Physics of Rocks*, 294 pp., Princeton Univ. Press, Princeton, N.J., 1994.

Gleason, G.C., and J. Tullis, A flow law for dislocation creep of quartz aggregates determined with the molten salt cell, *Tectonophysics, 247*, 1-23, 1995.

Gold, T., and S. Soter, Fluid ascent through the solid lithosphere and its relation to earthquakes, *Pure Appl. Geophys., 122* 492-530, 1985.

Gratz, A.J., Solution transfer compaction of quartzites - Progress toward a rate law, *Geology, 19*, 901-904, 1991.

Haar, L., J.S. Gallagher, G.S. Kell, *NBS/NRC Steam Tables: Thermodynamic and Transport Properties and Computer Program for Vapour and Liquid States of Water in SI Units*, 320 pp., Hemisphere, Washington, D.C., 1984.

Hacker, B.R., A. Yin, J.M. Christie, and G.A. Davis, Stress magnitude, strain rate, and rheology of extended middle continental crust inferred from quartz grain sizes in the Whipple Mountains, California, *Tectonophysics, 11*, 36-46, 1992.

Hanson, R.B., The hydrodynamics of contact metamorphism, *Geol. Soc. Am. Bull., 107*, 595-611, 1995.

Helle, A.S., K.E. Easterling, and M.F. Ashby, Hot-isostatic pressing: New developments, *Acta Metall., 33*, 2163-2174, 1985.

Holland, T.J.B., and R. Powell, An enlarged and updated internally consistent dataset with uncertainties and correlations, *J. Metamorph. Geol., 8*, 89-124, 1990.

Holness, M.B., Temperature and pressure dependence of quartz-aqueous fluid dihedral angles: The control of adsorbed H_2O on the permeability of quartzites, *Earth Planet. Sci. Lett., 117*, 363-377, 1993.

Kaufman, P.S., and L.H. Royden, Lower crustal flow in an extensional setting: Constraints from the Halloran Hills region, eastern Mojave Desert, California, *J. Geophys. Res., 99*, 15723-15739, 1994.

Kohlstedt, D.L., B. Evans, and S.J. Mackwell, Strength of the lithosphere: Constraints imposed by laboratory experiments. *J. Geophys. Res., 100*, 17587-17602, 1995.

Lasaga, A.C., Metamorphic reaction rate laws and development of isograds, *Min. Mag., 50*, 359-373, 1986.

Lasaga, A.C., and D.M. Rye Fluid flow and chemical reaction kinetics in metamorphic systems. *Am. J. Sci., 293*, 361-404, 1993.

Lockner, D., and B. Evans, Densification of quartz powder and reduction of conductivity at 700°C. *J. Geophys. Res., 100*, 13081-13092, 1995.

Manning, C.E., The solubility of quartz in H_2O in the lower crust and upper mantle, *Geochim. Cosmochim. Acta, 58*, 4831-4839, 1994.

McKenzie, D., The generation and compaction of partially molten rock. *J. Petrol., 2*, 713-765, 1984.

Nakashima, Y., Transport model of buoyant metamorphic fluid by hydrofracturing in leaky rock, *J. Metamorph. Geol., 13* 727-736, 1995.

Nishiyama, T., Kinetics of hydrofracturing and metamorphic veining, *Geology, 17*, 1068-1071, 1989.

Norris R.J., and R.W. Henley, Dewatering of a metamorphic pile, *Geology, 4*, 333-336

Norton, D., and R. Knapp, Transport phenomena in hydrothermal systems: Nature of porosity, *Am. J. Sci., 277*, 913-936, 1977.

Norton, D., and J. Knight, Transport phenomena in hydrothermal systems: Cooling plutons, *Am. J. Sci., 277*, 937-981, 1977.

Nur, A., and J. Walder, Hydraulic pulses in the Earth's crust, in *Fault Mechanics and Transport Properties of Rocks*, edited by B. Evans and T.-f. Wong, pp. 461-474, Academic, San Diego, Calif., 1992.

Palciauskas, V.V., and P.A. Domenico, Fluid pressures in deforming rocks, *Water Resour. Res., 25*, 203-213, 1989.

Paterson, M.S., The interaction of water with quartz and its influence in dislocation flow – An overview, in *Rheology of Solids and of the Earth* edited by S.I. Karato, and M. Toriumi, pp. 107-142, Oxford Univ. Press, New York, 1989.

Paterson, M.S., and F.C. Luan, Quartzite rheology under geological conditions, in *Deformation, Mechanisms, Rhe-*

ology and Tectonics, edited by R.J. Knipe and E.H. Rutter, *Geol. Soc. Spec. Publ., 54*, 299-307, 1990.

Peacock, S.M., Numerical constraints on rates of metamorphism, fluid production, and fluid flux during regional metamorphism, *Geol. Soc. Am. Bull., 101*, 476-485.

Raj, R., and M.F. Ashby, Intergranular fracture at elevated temperature, *Acta Metall., 23*, 653-665, 1975.

Raleigh, C.B., and M.S. Paterson, Experimental deformation of serpentinite and its tectonic implications, *J. Geophys. Res., 70*, 3965-3985, 1965.

Ramsay, J.G., The crack-seal mechanism of rock deformation, *Nature, 284*, 135-139, 1980.

Ranalli, G., *Rheology of the Earth*, 366 pp., Allen and Unwin, Winchester, Mass., 1986.

Ridley, J., Modelling of the relations between reaction enthalpy and the buffering of reaction progress in metamorphism, *Min. Mag., 50*, 375-384, 1986.

Rubie, D.C., The catalysis of mineral reactions by water and restrictions on the presence of aqueous fluid during metamorphism, *Min. Mag., 50*, 399-415, 1986.

Rutter, E.H., The kinetics of rock deformation by pressure solution, *Philos. Trans. R. Soc. London, Ser. A, 283*, 203-219, 1976.

Rutter, E.H., and K. Brodie, Mechanistic interactions between deformation and metamorphism, *Geol. J., 30* 227-239, 1995.

Schmid, R., Are the metapelites of the Ivrea-Verbano zone restites?, *Mem. Sci. Geol., 33*, 67-69, 1979.

Schramke, J.A., D.M. Kerrick, and A.C. Lasaga, The reaction muscovite + quartz = andalusite + K-feldspar + water, 1, Growth kinetics and mechanism, *Am. J. Sci., 287*, 517-559, 1987.

Scott, D., and D. Stevenson, Magma solitons, *Geophys. Res. Lett., 11*, 1161-1164, 1984.

Scott, D., and D. Stevenson, Magma ascent by porous flow, *J. Geophys. Res., 91*, 9283-9296, 1986.

Shaw, D.M., Geochemistry of pelite rocks, III, Major elements and general geochemistry, *Geol Soc. Am. Bull., 67*, 919-934, 1956.

Sibson, R.H., Earthquake faulting as a mineralizing agent in hydrothermal systems, *Geology, 15*, 701-704, 1987

Simpson, G.D.H., Dehydration-enhanced deformation during prograde regional metamorphism, NW Sardinia, Italy. *J. Metamorph. Geol.*, in press, 1997.

Skelton, A.D.L., C.M. Graham, and M.J. Bickle, Lithological and structural controls on regional 3-D fluid flow patterns during greenschist facies metamorphism of the Dalradian of the SW Scottish Highlands, *J. Petrol., 36*, 563-586, 1995.

Spiegelman, M., Flow in deformable porous media, 1, Simple analysis, *J. Fluid. Mech. 247*, 17-38, 1993a.

Spiegelman, M., Flow in deformable porous media, 2, Numerical analysis – The relationship between shock waves and solitary waves, *J. Fluid. Mech. 247*, 39-63, 1993b.

Stevenson, D., Spontaneous small-scale melt segregation in partial melts undergoing deformation, *Geophys. Res. Lett., 16*, 1067-1070, 1989.

Thompson, A.B., and J.A.D. Connolly, Migration of metamorphic fluid: Some aspects of mass and heat transfer, *Earth. Sci. Rev., 32*, 107-121, 1992.

Thompson, J.F., Grid generation techniques in computational fluid dynamics, *AIAA J., 22*, 1505-1523, 1984.

Thompson, P.H., Moderate overthickening of thinned sialic crust and the origin of granitic magmatism and regional metamorphism in low-P-high-T terranes, *Geology, 17*, 520-523, 1989.

Valley, J.W., and C.M. Graham, Ion microprobe analysis of oxygen in granulite facies magnetites: Diffusion exchange as a guide to cooling history, *Contrib. Mineral. Petrol., 109*, 38-52, 1991.

Vance, D., Rate and time controls on metamorphic processes, *Geol. J., 30*, 241-259, 1995.

Vrolijk, P., Tectonically driven fluid flow in the Kodiak accretionary complex, Alaska. *Geology, 15*, 466-469, 1987.

Waff, H.S., and U.H. Faul, Effects of crystalline anisotropy on fluid distribution in ultramafic partial melts, *J. Geophys. Res., 97*, 9003-9014, 1992.

Walder, J., and A. Nur, Porosity reduction and crustal pore pressure development, *J. Geophys. Res., 89*, 11539-11548, 1984.

Walsh, J.B., and W.F. Brace, The effect of pressure on porosity and the transport properties of rock, *J. Geophys. Res., 89*, 9425-9431, 1984.

Walther, J.V., and P.M. Orville, Volatile production and transport in regional metamorphism, *Contrib. Mineral. Petrol., 79*, 252-257, 1982.

Wanamaker, B.J., T.-f. Wong, and B. Evans, Decrepitation and crack healing of fluid inclusions in San Carlos olivine, *J. Geophys. Res. 95*, 15623-15642, 1990.

Wiggins, C., and M. Spiegelman, Magma migration and magmatic solitary waves in 3-d, *Geophys. Res. Lett., 22*, 1289-1292, 1995.

Wilkinson, D.S., and M.F. Ashby, Pressure sintering by power law creep, *Acta Metall., 23*, 1277-1285, 1975.

Wong T.-f., S-c. Ko, and D.L. Olgaard, Generation and maintenance of pore pressure excess in a dehydrating system, 2, Theoretical analysis, *J. Geophys. Res. 102*, 841-852, 1997.

Yardley, B.W.D., Fluid migration and veining in the Connemara Schists, Ireland, in *Fluid-Rock Interactions During Metamorphism* edited by J.V. Walther and B.J. Wood, pp. 89-108, Springer-Verlag, New York, 1986.

Yardley, B.W.D., and G.E. Lloyd, Why metasomatic fronts are really sides, *Geology 23*, 53-56, 1995.

Young, E.D., and D. Rumble, The origin of correlated variations in in-situ $^{18}O/^{16}O$ and elemental concentrations in metamorphic garnet from southeastern Vermont, USA, *Geochim. Cosmochim. Acta, 57*, 2585-2597, 1993.

Zhang, S., M.S. Paterson, and S.F. Cox, Porosity and permeability evolution during hot isostatic pressing of calcite aggregates, *J. Geophys. Res., 99*, 15741-15760, 1994.

Zhu, W., C. David, and T.-f. Wong, Network modeling of permeability evolution during cementation and hot isostatic pressing, *J. Geophys. Res., 100*, 15451-15464, 1995.

J. Connolly, IMP-ETHZ, Zurich 8092, Switzerland. (e-mail: jamie@erdw.ethz.ch)

(Received June 19, 1996; revised January 20, 1997; accepted March 3, 1997.)